SAND2013-3088C

SYNTHESIS, MICROSTRUCTURE, AND EXPLOSIVE PROPERTIES OF SPRAY-DEPOSITED SILVER ACETYLIDE-SILVER NITRATE COMPOSITE LIGHT INITIATED HIGH EXPLOSIVES

Timothy T. Covert and Marcus A. Chavez
Energetic Materials Simulations and Fabrication, Dept. 2556
Sandia National Laboratories
P.O. BOX 5800
MS1454 & MS1452
Albuquerque, NM 87185, USA
Email: ttcover@sandia.gov & mchav12@sandia.gov

ABSTRACT

Previous studies of pure silver acetylide-silver nitrate (SASN) showed that the synthesis route crash precipitates two distinct particle structures as seen with a scanning electron microscope, while the spray-deposition process yielded a high porosity product. Raman, infrared, and energy-dispersive X-ray spectrometry show a complex dispersion of different molecules. The light initiated high explosive was altered during synthesis using a nonreactive flouroelastomer terpolymer, Viton B600, and with a non-ionic surfactant, Triton X-100, in order to investigate the effects to the microstructure and subsequent effects on detonation phenomena. SASN slurry was made, but with five percent mass fraction of the Viton B600 mixed after synthesis, with the idea to better adhere the particles together in a uniform matrix and partially degrade the explosive performance to achieve higher resolution in deposition. A four percent mass fraction of the Triton X-100 surfactant was dissolved in acetonitrile prior to reacting with final ingredients for the SASN explosive in hopes of controlling the particle size, morphology, and to sterically stabilize the explosive slurry before spraying to achieve a higher bulk density. The two composite explosives were compared to pure SASN in terms of microstructure and explosive output.

Sandia National Laboratories is a multi-program laboratory managed and operated by Sandia Corporation, a wholly owned subsidiary of Lockheed Martin Corporation, for the U.S. Department of Energy's National Nuclear Security Administration under contract DE-AC04-94AL85000.

INTRODUCTION

Silver Acetylide-Silver Nitrate (SASN) explosive was developed for use as a Light Initiated High Explosive (LIHE) to impart a simultaneous material and structural response to a test article of a simple or complex geometry. The established processing and application technique for SASN requires synthesizing the explosive into a slurry that can be spray-deposited onto a thin layer of already spray-deposited Viton B, which is applied directly onto a test article's surface before explosive application to aid in adherence. The explosive is "sun-tanned" with ultraviolet light to aid in adsorbing radiant light energy. The article with the SASN explosive is then subjected to intense light irradiation, detonating it, and imparting an impulsive load to the structure. The direct spray process cannot currently achieve material response for most materials due largely to the low density and thin layer of the spray-deposited explosive. In order to excite material responses in materials of interest, a development effort at the Light Initiated High Explosives Facility at Sandia National Laboratories (SNL) in Albuquerque, New Mexico utilizes SASN to drive a precisely spaced thin flyer plate into a target. The flyer plate technique allows for control over the pulse width by changing the thickness of the plate and adjustment of the acceleration gap between the plate and impact surface of the test article. A correct combination of the flyer material and impact velocity controls the peak pressure delivered to a target surface. Below, Figure 1 shows the one-dimensional experimental set-up of this research's flyer plate tests.

Currently, the LIHE Gurney models for determining the maximum velocity of a flyer plate given a measured mass of explosive, agrees well with experimental data in a few flyer plate experiments, but not in the overwhelming majority of experiments. Flyer velocity data also has significant scatter for a given areal density, or areal mass, of explosive deposited. A previous study pointed to transient detonation phenomena and non-uniformity of SASN causing the scatter and non-applicability of the Gurney model [1]. This study modified SASN with a surfactant and a phlegmatizer in hopes to better control the flyer plate velocity for a given mass of explosive.

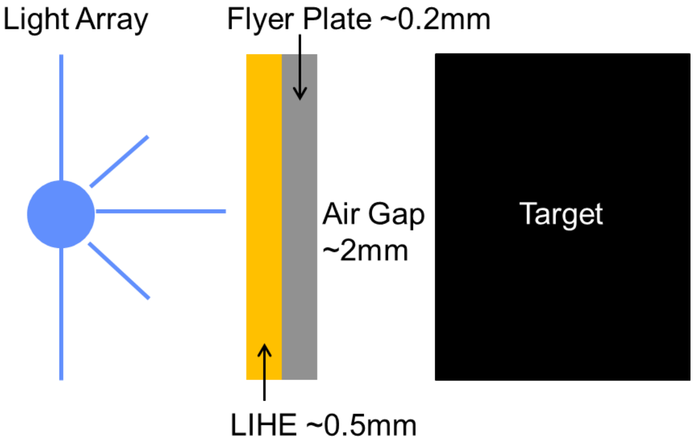

Figure 1, Illustration of the one-dimensional explosive/flyer/target setup and some typical values for thicknesses of different elements. NOTE: Not to Scale.

BACKGROUND

LIHEs are characterized by their initiation, attributed to the photo-thermal effect [2-4], and their extreme sensitivity to all other initiation mechanisms such as shock, friction, heat, and other sources of energy since they are considered primary explosives. Experimenters suspect that the exposed layers of explosive are initiated when high energy photons scatter within the subsurface, and excite electrons that in turn cause phonons to form, heating the energetic material to ignition [2-4]. Figure 2 attempts to qualitatively describe the ignition of a LIHE. Under intense light irradiation, hundreds of discrete initiation points per square centimeter are seen on witness plates covered in LIHE residue indicating the relative simultaneity of ignition over the exposed surface [5]. The induction time of the particular LIHE, SASN, is on the order of 10-μs, with the light sources used at the SNL LIHE Test Facility, before most diagnostics register any motion [6].

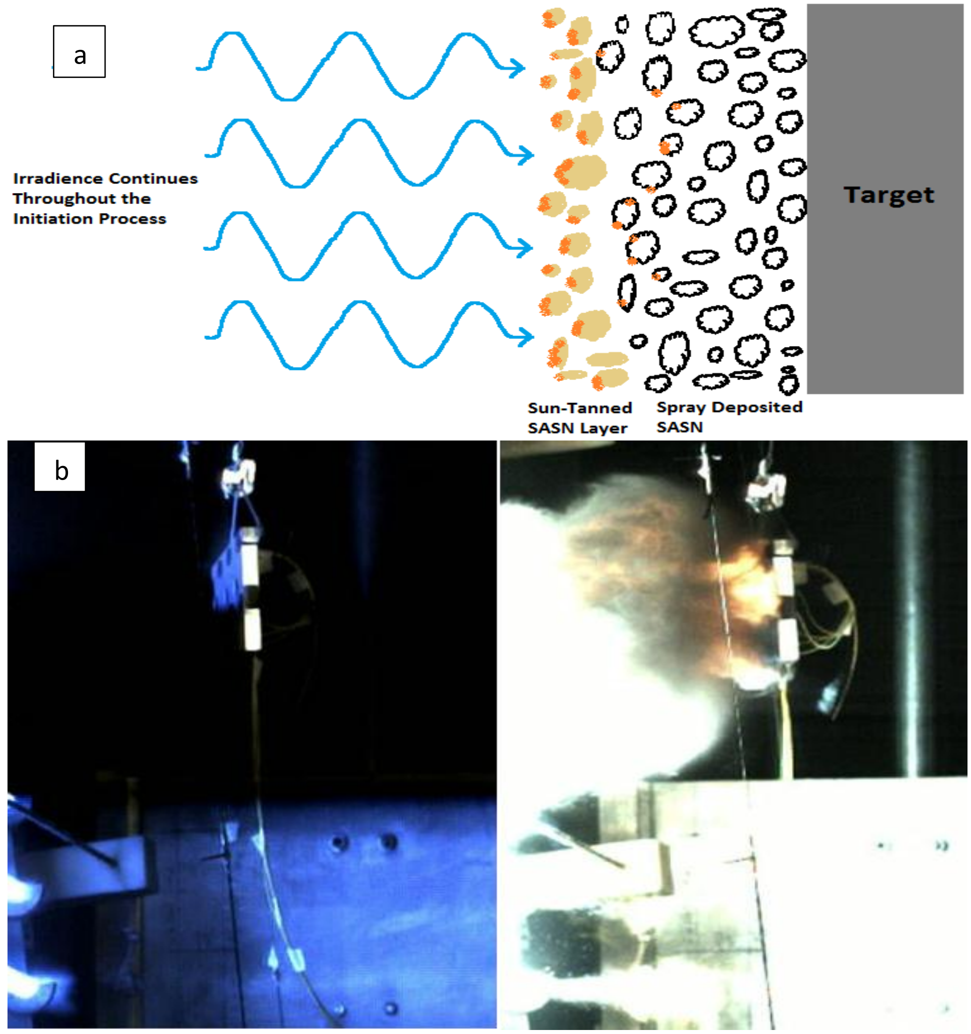

Figure 2, a) Incident photons strike the exposed outer surfaces of the LIHE particles, in this case SASN, and are adsorbed to the electronic skin depth, causing phonons to induce hot spot (orange colored spots) formation. Thermal explosion follows from these discrete points that may actually be more of a volume of particles because of the high porosity [1]. b) High-speed photography of light array irradiating a target in one frame then detonation in the following frame on right.

These explosives usually have heavy metals such as silver or lead attached to some chlorine, nitrogen, oxygen complex, or combination thereof. Upon ignition, LIHEs likely follow most of the same governing chemistry and physics as conventional carbon-hydrogen-nitrogen-oxygen (CHNO) explosives, but the properties have not been extensively studied. Figure 3 reveals the morphology of SASN particles under the high magnification of a scanning electron microscope (SEM). At a density of 5.34-g/cm^3, SASN is reported to have a steady-state detonation-velocity of 4450-m/s [6]. The as-sprayed state reports of 600 to 1500-m/s for the sweeping detonation-velocities of several batches of SASN have been recorded [5-8].

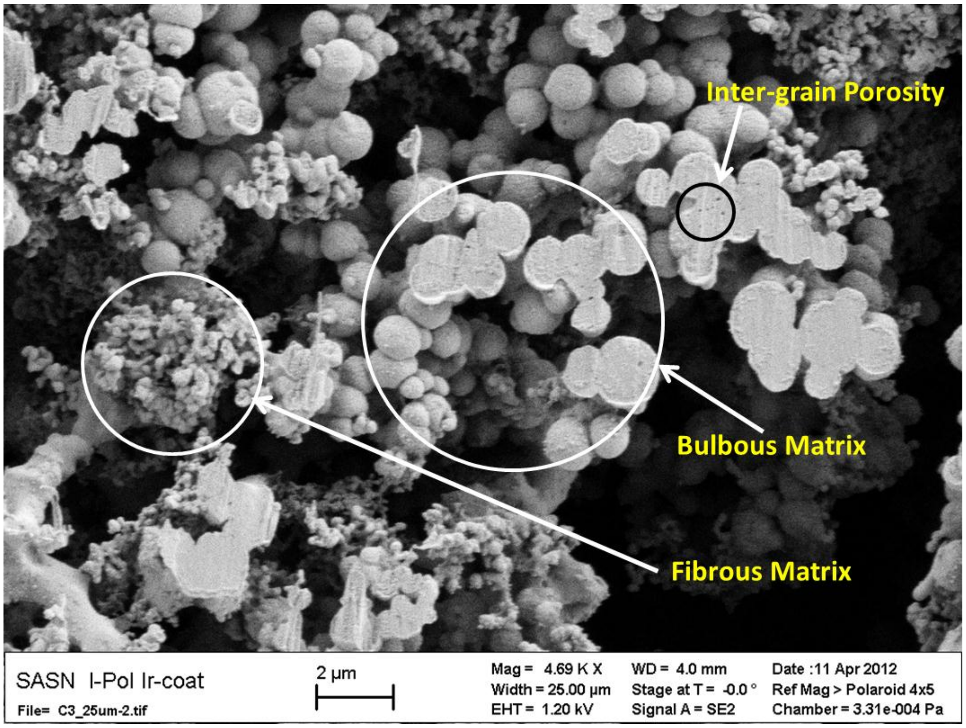

Figure 3, Cross-sectioned and spray-deposited silver acetylide-silver nitrate explosive under a FE-SEM showing a very porous structure composed of two distinct particle size distributions and morphologies [1]. The pores within the bulbous matrix are on the order of 50-nm or less. Large spherical bulbous particles are on the order of 0.5-2-µm while the fibrous matrix of particles is on the order of 0.1-µm in diameter and ~0.5-µm in length.

Silver Acetylide-Silver Nitrate Synthesis

SASN synthesis is relatively simple chemistry wise, but requires extreme caution due to the sensitivity of the final product. The explosive is remotely synthesized at the LIHE Facility with all reactants behind blast shields and under conditions inhibiting the propagation of detonation by liquid phlegmatization. Most explosives cannot sustain a detonation in the presence of a chemically non-reactive liquid as long as the explosive is dilute. The LIHE Facility method for preparation of the sensitive explosive is consistent and helps ensure a high purity product using certified reactants, while controlling the ambient environment. The simple chemical equation is shown below in Eq. (1):

$$3AgNO_3(\text{in solution}) + C_2H_2(\text{gas}) \rightarrow Ag_2C_2 \cdot AgNO_3(\text{precipitate}) + 2HNO_3(\text{liquid}) \tag{1}$$

Acetylene (C_2H_2) is bubbled through an agitated solution of silver nitrate ($AgNO_3$) dissolved in acetonitrile for 30 minutes to produce the precipitant of 1:1 SASN molecules [6]. Figure 4 shows the 1:1 SASN molecular arrangement of silver atoms and suspended carbon atoms that would comprise a grain or particle of the explosive [9].

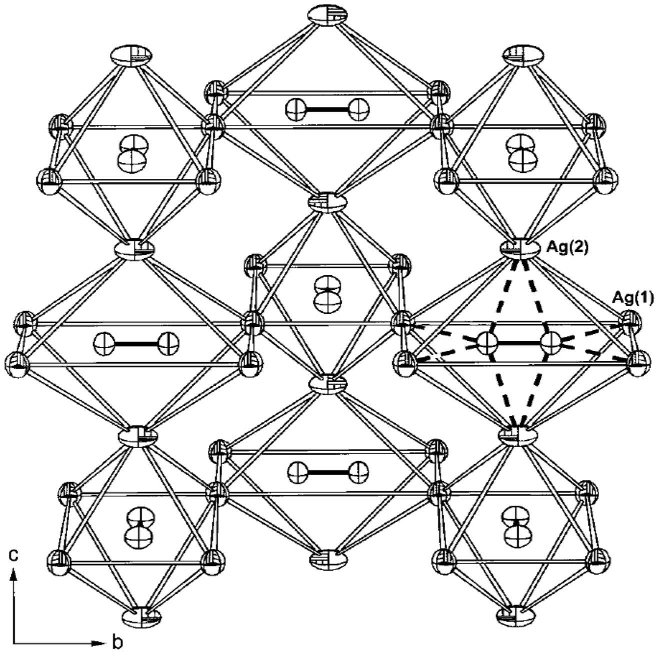

Figure 4, The molecular assembly of 1:1 SASN molecules as assumed for the current formulation process [9]. The Ag cages house the suspended triply bonded carbon atoms (center of each cage) and the NO_3 molecules occupy the spaces between the Ag cages. Reprinted with permission from reference 9. Copyright 1999 American Chemical Society.

After precipitation, the supernatant liquids of nitric acid (HNO_3) and acetonitrile (C_2H_3N) are decanted off then washed out with acetone (C_3H_6O) multiple times. Acetone is added once again and becomes the carrier fluid for the resulting slurry of SASN that is approximately 10.2% solids mass loading in a large 4000-mL beaker. The resulting precipitate of SASN seen during formulation is shown in Figure 5. The humidity is controlled to 35% ±10% and a temperature of 80°F ±3°F is maintained within the formulation/spray booth. A previous paper best describes the remaining sun-tanning, spraying procedures, and target preparation that are necessary to ensure a quality coating of detonable LIHE onto a target surface [1].

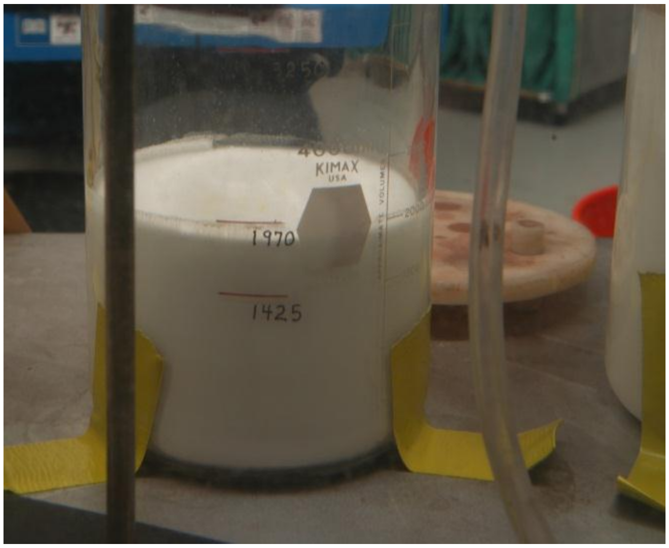

Figure 5, One batch of silver acetylide-silver nitrate explosive in slurry form under strong agitation by rotating stir bar remotely mixed at the SNL LIHE Facility for TP48.

Figure 6, Cylindrical spray operation in progress for TP48. The first few layers of SASN appear white and completely cover the flyer plate and direct spray samples. This the same set up used for shot series TP49, which is the focus of this study.

EXPERMENTAL TECHNIQUES AND PROCEDURES

Three batches of pure SASN, 4% Triton X-100/SASN, and 5% Viton B600/SASN were synthesized as explained above and sprayed onto three cylindrical targets that were covered by a flyer plate stretching a quarter of the perimeter and another quarter perimeter were covered with diagnostics to directly measure detonation phenomena. Diagnostics for the flyer plate included flyer plate velocity tracking via photonic Doppler velocimetry (PDV) and VISAR are best explained in references 10-14. Direct detonation interrogation techniques included front-surface particle velocity (FSPV) and embedded fiber optic sensors (EFOS), which will be further explained in Figs. 7-10 and the following paragraphs. In addition to the mentioned diagnostics, areal density or mass per area was measured and thickness measured with an optical comparator to determine bulk densities of each explosive.

Flyer Plate Velocity Tracking

Each cylindrical ring had five laser interferometers to record the velocity profiles produced by the deflagration/detonation of the above mentioned LIHEs. Two of the diagnostics were PDV and the rest were VISAR, which are both accurate and complimentary velocity determination techniques. The PDV system uses the Doppler shift and a beat frequency of reflected light (reflected from a spectral surface) as compared to a reference leg of the laser source with a heterodyned signal [11-14]. The sensitivity for the detectable amount of displacement is half the wavelength of the laser source for a minimum of sub-nanoseconds [14]. The LIHE Facility PDV system uses a 1550-nm wavelength laser, which can detect 775-nm of normal displacement from a spectral surface [12-14]. The infrared detectors have a 2-GHz bandwidth and the digitizers were 2.5-GHz bandwidth. With a heterodyned signal, the PDV system has a working range of measurable velocities from less than 0.1-m/s to 387.5-m/s as long as the signal to noise ratio is greater than one, especially in the low velocity regime [14]. Working distance PDV probes of 29-mm are made by OZ Optics were used in all experiments of this study. The actual fiber optic is composed of fused silica batched and drawn at DuPont with a 9-µm inner core diameter and outer core diameter measured at the LIHE facility to range from 120.7 to 129.5-µm. The specific probe model used was LPF-04-1550-9/125-S-4-29-6.2AS-60-3A-1-1 for flyer velocity measurements and FSPV.

The PDV probes are mounted behind BK7 glass windows that are anti-reflection coated to avoid extraneous reflected laser light from entering back into the fiber. The windows are 3-mm thick X 12.7-mm in diameter. An illustration of the experimental set-up is shown below in Fig. 7. The VISAR standard hypodermic needle probes are ultraviolet light cured with a special adhesive as noted in Fig. 8. The window used in this case is a 0.5-mm X 6.4-mm diameter polycarbonate optical material. The LIHE facility VISAR system has a fringe constant equal to 123 m/s/fringe.

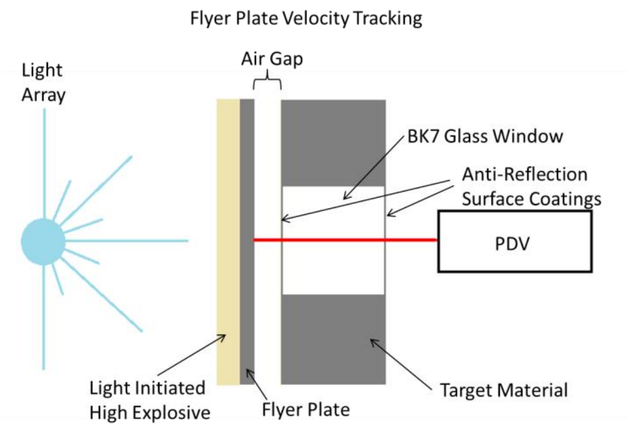

Figure 7, Cross-sectional view of flyer plate tracking with PDV. A probe holder is epoxied to the window and target, which allows for optimizing the light return in-situ before gluing the PDV probe in place.

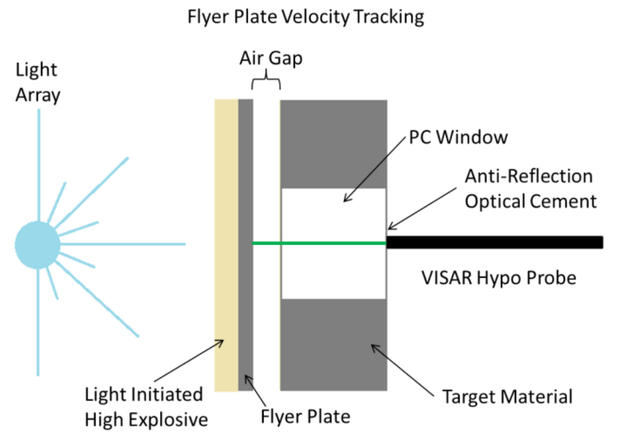

Figure 8, Cross-sectional view of flyer plate tracking with VISAR. Norland Optical Adhesive 68 is used to glue the VISAR probe directly to the polycarbonate window.

Front-Surface Particle Velocity

Particle velocity can easily be measured using the PDV laser interferometer technique mentioned above, but with a few adjustments in the experimental set-up as noted in Fig. 9 below. Explosive is detonated in direct contact with the spectral surface, inducing a particle velocity jump (if it is truly detonating) into the window material. Measurement of this jump allows for use of a special equation called the Deal equation [15], to be used to approximately determine the pressure spike in the explosive. The Deal equation is shown below as Eq. (2):

$$P_{spike} \approx 5u_w(\rho_{HE}D + \rho_w U_w) \qquad \text{Eq. (2)}$$

Where:
P_{spike}=Last pressure spike in high explosive undergoing detonation (kbar)
u_w=Measured window velocity corrected for shock induced change in the index of refraction if necessary (mm/µs)
U_w=Calculated or measured window shock velocity (mm/µs)
ρ_w=Assumed or measured window bulk density (g/cm^3)
ρ_{HE}=Assumed or measured high explosive bulk density (g/cm^3)
D=Measured or assumed detonation velocity (mm/µs)

The accuracy of this equation for determining the spike is a matter of having a well-defined shock Hugoniot for the optical window, the HE bulk density, detonation velocity at the time of window interaction, thinnest possible spectral coating, and high bandwidth detection systems. Also, the shock impedance of the window material must be close to the shock impedance of the detonation products. This is assuming that the experiment is truly one-dimensional in detonation propagation and coupling of the induced shock is perfect. A detonation wave has a specific structure in one-dimension and steady-state propagation as shown in Fig. 10. Ideally, this diagnostic should be able to measure the von Neumann spike since this is the easiest feature to pick out from a particle velocity trace. However, coupling a normal propagating detonation wave, not allowing the quickly decaying peak particle velocity (or pressure) to drop, and having a high enough bandwidth detection system are difficult feats to accomplish as with any other diagnostic technique. The Chapman-Jouguet pressure is easier to measure in terms of actually recording it and not decaying the wave peak, but knowing where the exact location of this special point exists in the recorded trace is a best guess. The Chapman-Jouguet point is the end of the reaction zone in an ideally steady-wave detonation that divides the supersonic compression wave from the subsonic rarefaction wave, also known as the Taylor wave [16].

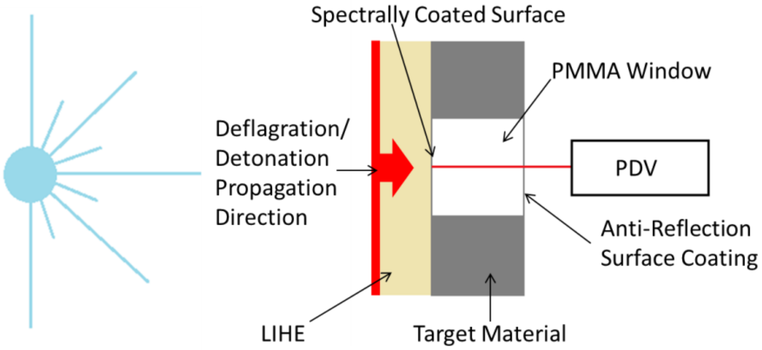

Figure 9, Front-surface particle velocity diagnostic cross-sectional view. PDV can be substituted with VISAR or another laser interferometer technique, but this was the experimental set-up for shot series TP49. Note that the window material is polymethyl methacrylate (PMMA).

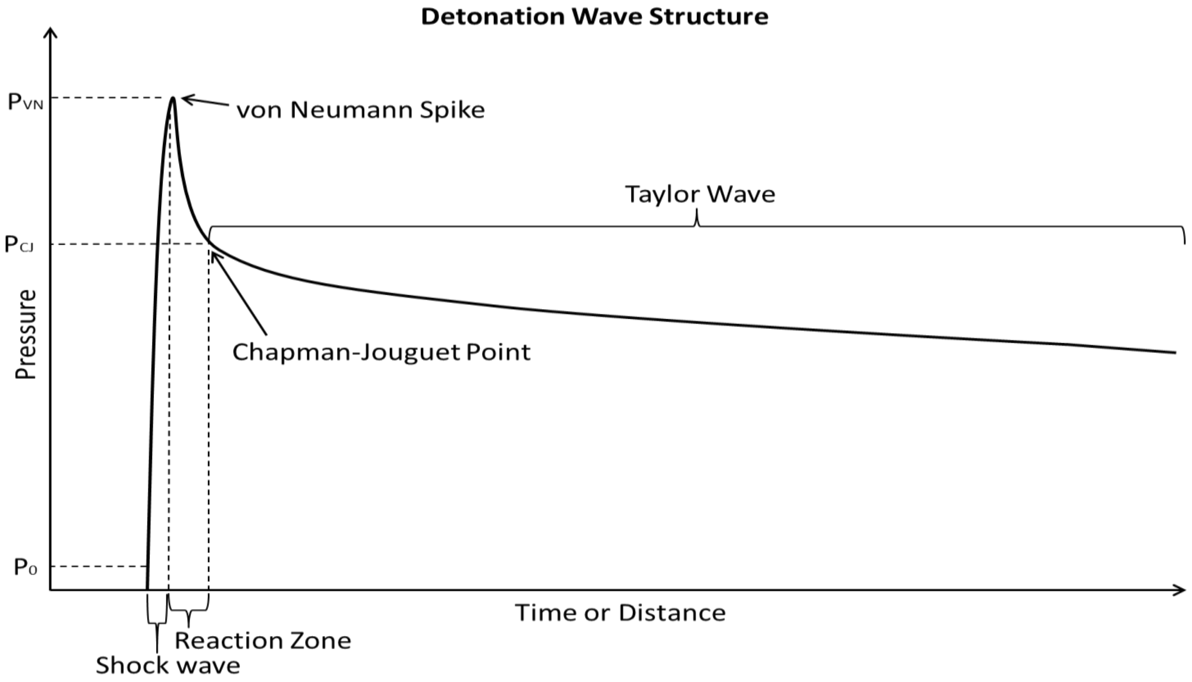

Figure 10, Zel'dovich, von Neumann, and Döring (ZND) model of steady-state detonation wave structure in ideal high explosives [16]. Explosives typically detonate while at ambient atmospheric pressure, P_0. The ambient pressure is minuscule in comparison to both the von Neumann and Chapman-Jouguet pressures. Particle velocity traces match the pressure traces until since most particle velocity to pressure correlations are nearly linear based on data collected at the LIHE facility.

Each ring had only one FSPV measurement due to PDV channel availability. The PMMA windows were 5.35-mm thick X 12.7-mm diameter PMMA optical windows. There was an anti-reflective coating on the PDV probe-side face and the laser light reflects off of a Physical Vapor Deposition (PVD) mirror. The PVD layer was composed of 3000-Å thick aluminum and 500-Å of titanium at the window/spectral surface interface for adhesion. An aluminum oxide layer approximately 500-Å was deposited over the aluminum spectral surface to aid in durability of the coating. PMMA was chosen because there is very little shock-induced change in index of refraction [17], the shock Hugoniot is well known [17], and the shock impedance is on the same order as the detonation products of SASN based explosives. Figure 11 below depicts the FSPV diagnostic outside of a ring target and inside of one.

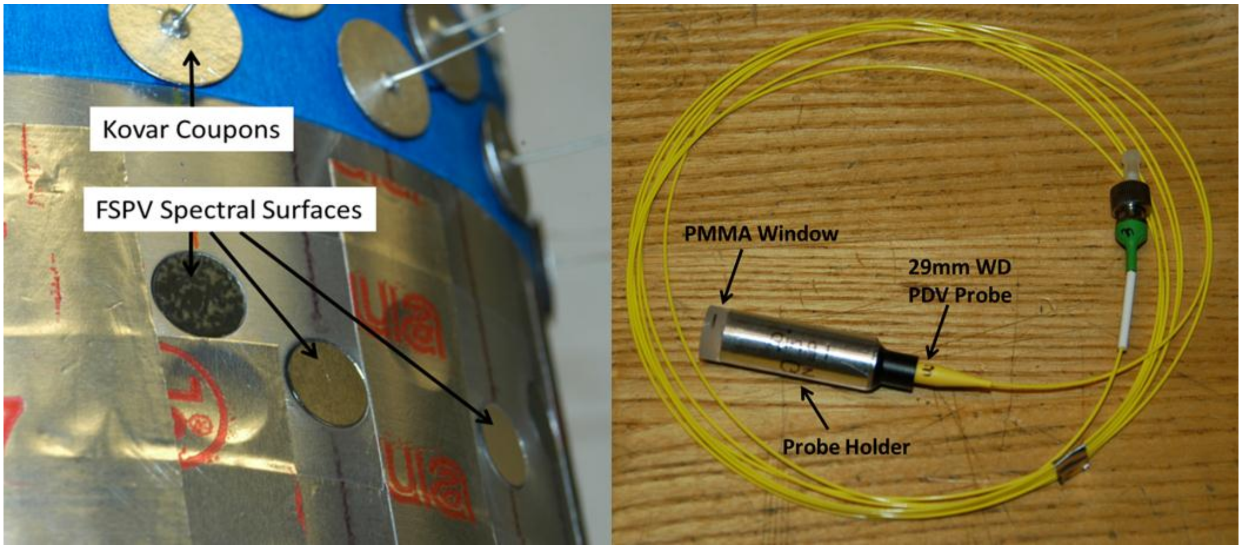

Figure 11, Left photo shows a ring test sample from shot series TP48 and was very similar to that of TP49. Kovar coupons are placed near the spectral surface of the FSPV and other diagnostics in order to obtain the thickness, areal density, and bulk density of the explosive. The splotches of Viton B can be seen on the mirrored surfaces, which are spray-deposited with the Viton B prior to main explosive application. Right photo shows the FSPV without the PDV probes installed or Viton B.

Embedded Fiber Optic Sensors

A newly developed and recently implemented diagnostic at the LIHE facility utilizes the same concepts as the FSPV, but on the micro-scale. The detonation velocity of SASN has historically been measured in the same manner as other explosives; with a strip of the explosive initiated on one end and time-of-arrival pins at known distances from the ignition point [5-8]. This type of measurement is great for determining steady-state sweeping waves, but neglects the nearly one-dimensional unsteady wave propagation that a LIHE can offer in 500-µm or less since the LIHE ignites from the exposed outer surface and burns towards the substrate it is spray-deposited onto. In order to effectively measure the deflagration/detonation velocity of SASN based LIHEs; four fibers in a rosette arrangement on each cylindrical ring target were placed adjacent to the FSPV diagnostic and had a corresponding Kovar coupon nearby. The illustrations and photographs in Figs. 12 and 13 shows the diagnostic as it was employed in test series TP49.

The newly developed diagnostic is called embedded fiber optic sensors (EFOS) as mentioned in an earlier paragraph. Corning SMF-28 9/125-µm diameter fibers are plane-cleaved and were spectrally coated with 4000-Å of aluminum for Rosettes 1 and 2 with a 1-in segment of fiber jacket cut away to expose the coated fiber tip. Rosette 3 had a different coating of 500-Å titanium for adherence between the fiber tip and the 3500-Å thick aluminum spectral surface. Over the aluminum was a 1000-Å layer of aluminum oxide to act as a protective coating. Besides detecting time-of-arrival data, the probes were expected to produce particle velocity traces similar to FSPV, but three-dimensional effects of converging shocks/detonation waves, rarefactions, explosive jetting, and the shock-induced change of the index of refraction must be considered and quantified in order to produce actual particle velocity and pressure-time histories. The apparent particle velocity time-history was recorded to help find the deflagration-to-detonation transition (DDT) of each explosive mix investigated. Other caveats to be considered are how much explosive is actually deposited over the top of each fiber, and although light initiation is nearly simultaneous over small areas, what is the simultaneity of ignition over each fiber tip? In other words, how planar is the wave when it interacts with the fiber tip?

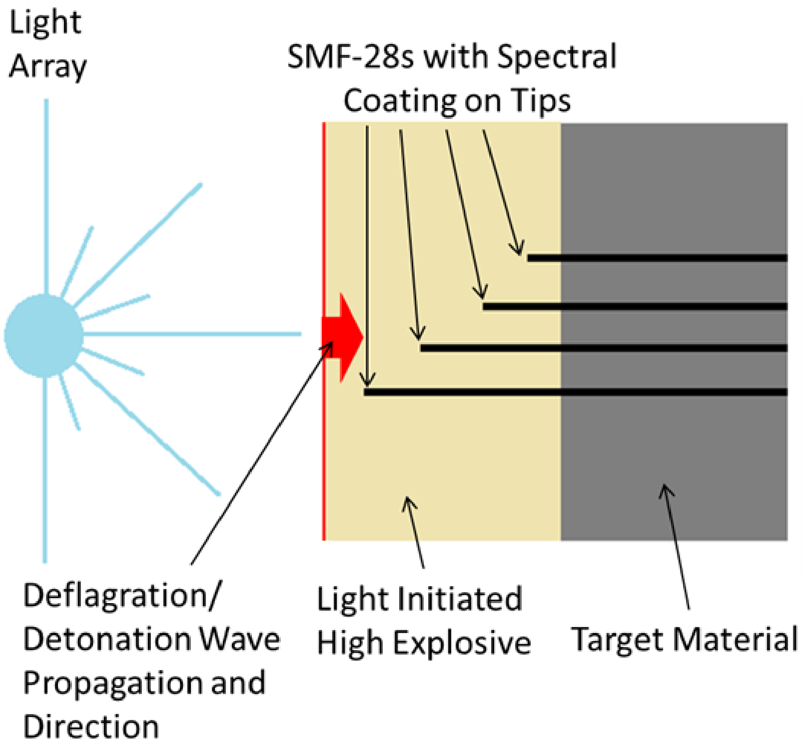

Figure 12, Expected cross-sectional view of the EFO TOADs when over-sprayed by LIHE. The tips are as perpendicular to the surface to be sprayed and the elevation above this surface is precisely set and measured with an optical comparator to within ±0.00005-in (±1.27µm). The fibers feed back into the PDV system thus measuring the response with a 100-ps time resolution with the current LIHE facility digitizers and detectors.

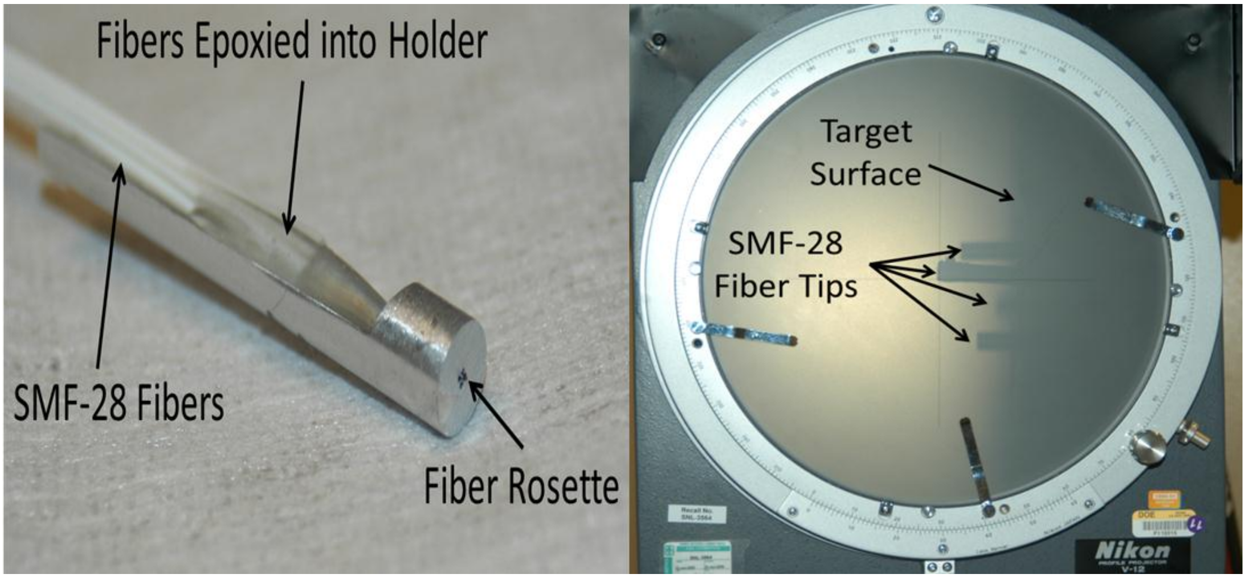

Figure 13, Left photo is the final assembly of a fiber rosette ready to be installed into a cylindrical ring target. The four fibers protrude out of four 17-mil diameter drilled holes. Right photo shows same fiber rosette under an optical comparator with the longest fiber in focus.

Specific Impulse Measurement

The LIHE facility utilizes a ballistic pendulum to measure the imparted impulse from SASN as a function of areal density. Every test day during a shot series has five Kovar coupon quality control samples that are fired on a smaller light array to ensure that the explosive manufactured is at least within the measurement bounds. These bounds are the error of the specific impulse equations developed from a statistical database of pure SASN impulse data. The equations for the SASN specific impulse are beyond the scope of this study. The coupons fired were chosen according to their areal density in order to have an impulse measurement in all regions of flyer plate sample depositions to be fired that day.

Bulk Density and Thickness Uniformity

Average bulk density was measured on multiple test series with Kovar coupons and a shadow-graphing technique with an optical comparator. The direct measurement of the total thickness of the SASN plus the Viton B and coupon thickness aided in calculation of the bulk density. The thickness of the coupon before and after the application of Viton B was necessary to measure in order to complete the bulk density determination of the sample. Thickness measurements were made at four locations 90° from each other near the perimeter of the coupon giving the average bulk density as a function of the areal density of explosive deposited.

Scanning Electron Microscopy Analysis

Field emission scanning electron microscopy (FE-SEM) was employed with a Zeiss SUPRA 35VP to investigate the matrix properties of spray-deposited material [18]. One SEM sample per batch of composite LIHEs and pure SASN were ion polished, or ion beam nano-tomography, with a JEOL ion polisher with a 4kV argon ion beam for 4-6 hours before taking images to gain insight on the internal lattice structure of SASN [18]. The samples from each explosive batch were sprayed onto small stages specially designed to allow the cross-sectioning by an ion beam and for investigation within the variable pressure FE-SEM.

Energy Dispersive X-Ray Spectroscopy Analysis

Coupled with the FE-SEM is an EDS device, or energy dispersive X-ray spectrometer, to measure the fluoresced X-rays from the elements within the sample. These fluoresced X-rays have been correlated with known standards, which allow for elemental and compound determination of a sample [18,19]. Elemental and compositional analysis maps were produced to show the relative homogeneity of the explosives.

Raman and Infrared Spectroscopy Analysis

Vibrational spectroscopy was performed on all three LIHEs with both Raman and infrared (IR) spectrometers. These machines use laser energy to excite and vibrate the molecules to resonant frequencies that are compared to standards, which give both relative qualitative and quantitative compound data [20]. The instruments and the settings are presented below [21]:

Raman instrument

Witec Alpha300R
Laser: 785-nm, set at ~25% of maximum power
Region 840-2420-cm^{-1}
Aperture: 100-µm fiber
Objective: 20X Zeiss, infinity corrected
Integration time: 0.75-sec, 8 scan average
Grating: 600-g/mm

Infrared instrument

Bruker Vertex 70v, Hyperion Microscope
Infrared Microscope: 20x objective, Reflectance Mode

Detector: MCT
Resolution: 4-cm^{-1}
Co-Adds: 32
Reference: Reflective Gold Surface

Each of the three samples was mapped similarly to Fig. 14 to acquire data collection from multiple areas to investigate the homogeneity of the samples for both Raman and IR spectroscopy. These analysis techniques were necessary since EDS is limited to determining elements and compounds, but cannot determine the nature of the bond energy. SASN molecules are theorized and measured to have triply bonded carbon atoms that hold the complex salt of silver acetylide to silver nitrate together [9].

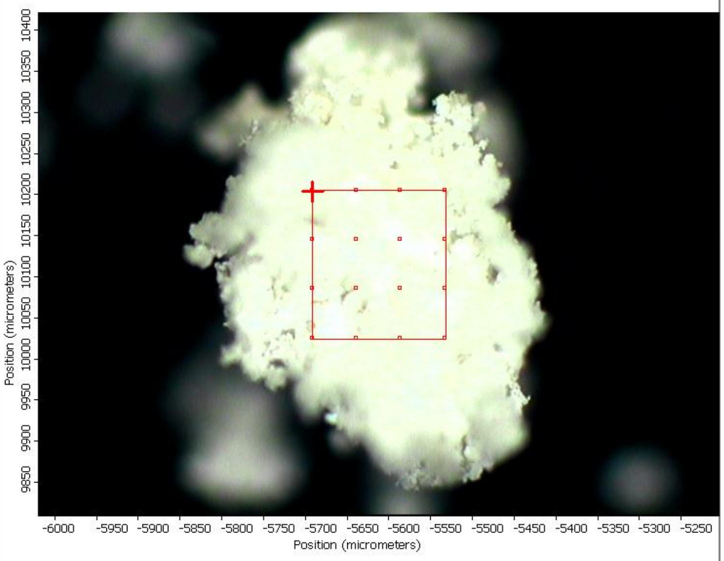

Figure 14, Pure SASN sample from shot series TP48 mapped out for infrared spectroscopy. Each red dot represents the area investigated [22].

RESULTS AND DISCUSSION

Flyer Velocity Profiles

An image of the how the target ring looks during a detonation of an LIHE is shown in Fig. 15. All fifteen flyer velocity profiles were captured and are shown below in Figs. 16-18. The velocity profiles have distinct features that tell much about the explosive driving the flyer plate, the air trapped between the target and the flyer plate, and the ignition simultaneity. The initial acceleration phase contains the most information about the pressure pulse applied to the flyer plate by the explosive. The deceleration phase before window impact is due to trapped air. Ignition simultaneity is seen as the plate launch-offs and varies between 5 and 10-µs, which are due to the fact that the light array is a planar arrangement instead of better matching the cylindrical geometry of the target rings. Light will scatter more because much of the incident photons are striking the exposed explosive surface at glancing angles for the lower flyer plate velocity cases, PDV2 and VISAR3 according to the legends in Figs. 16-18.

Ring 2 in Fig. 17 has an interesting velocity profile as pointed out in the figure. PDV2 shows a max velocity early in flight preceding a quick velocity decay with a subsequent velocity rise to a slightly lower max velocity prior to window impact. This indicates a quick transfer of momentum from the explosive early on with another momentum transfer from the detonation products later in flight. This is seen in almost all velocity profile traces where there are multiple acceleration phases and is described in another paper [1].

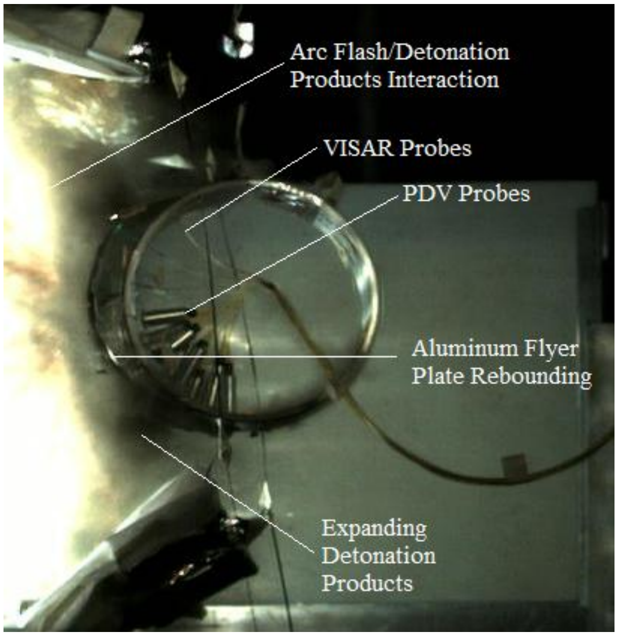

Figure 15, A cylindrical flyer plate test from test series TP46. The still photo is from a high speed camera and shows the same experimental configuration for the light array and target ring placement as was used in test series TP49.

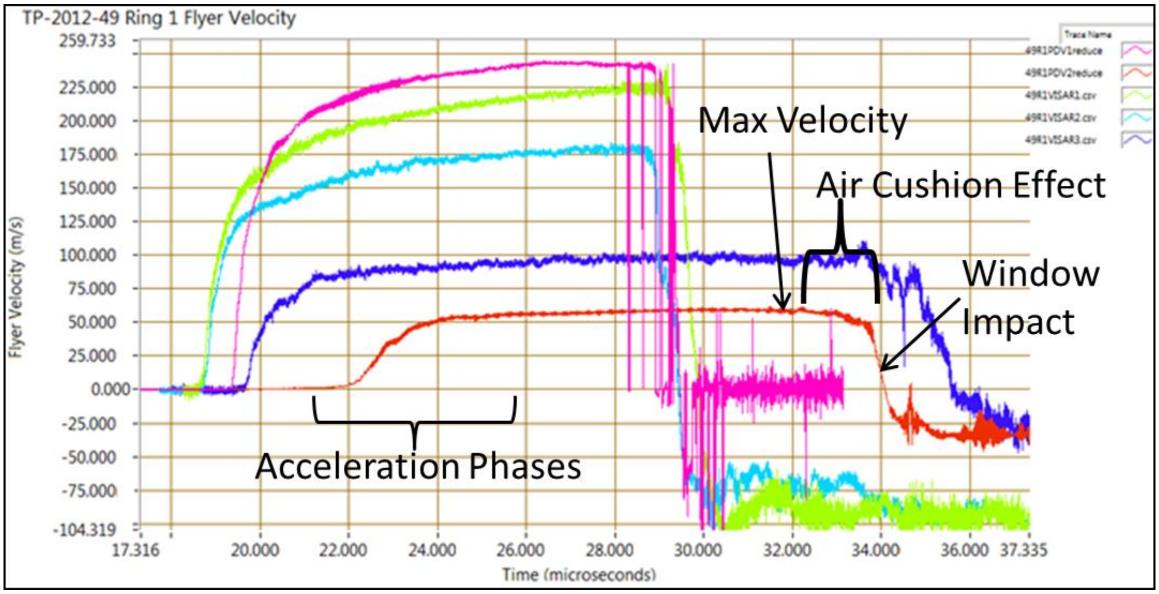

Figure 16, Pure SASN flyer velocity profiles measured by both PDV and VISAR diagnostics. The PDV2 trace is broken down into distinct regions, which are used for final interpretation of data.

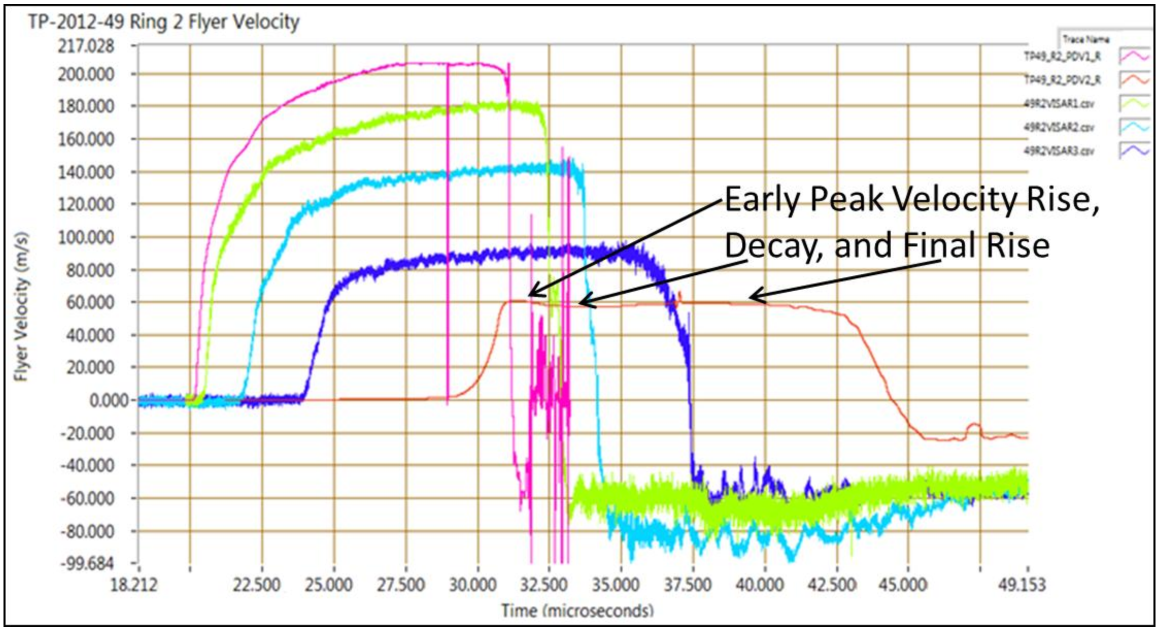

Figure 17, 4% Triton X-100/SASN flyer velocity profiles as measured with PDV and VISAR. Notice the PDV2 trace has an interesting profile as pointed out in the figure.

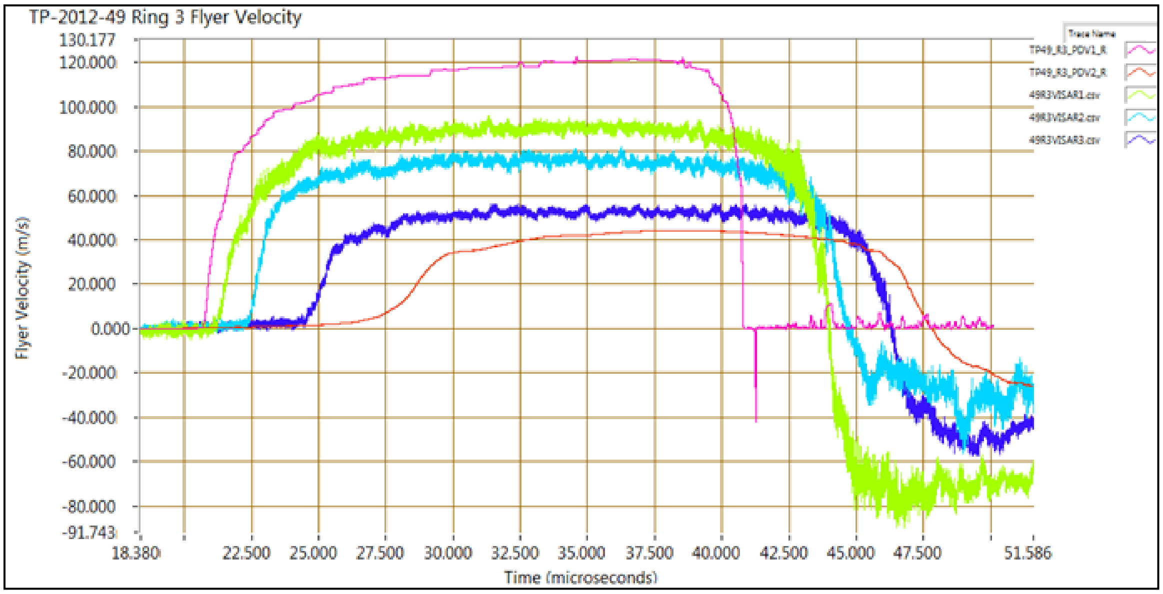

Figure 18, 5% Viton B600/SASN flyer velocity profiles as measured with PDV and VISAR.

The pure SASN batch, or Ring 1, had the highest achieved maximum flyer plate velocities, followed by the Triton X-100/SASN batch, Ring 2, and lastly by the Viton B600/SASN batch deposited on Ring 3 as is shown in Fig. 18. Ring 1 only had one coupon adjacent to the flyer velocity diagnostic, while Rings 2 and 3 had two adjacent coupons. This is important because there is considerable spread between the two coupons at almost every flyer velocity, meaning that weighing coupons introduces error with knowing how much explosive was actually deposited over the flyer velocity diagnostic. The Viton B600 doped SASN seems to accentuate this most likely because the explosive adheres better to surfaces, such as the stem and back of the Kovar coupon. The areal density scatter on Ring 2 coupons is minimal because the Triton X-100 did not seem to change this explosive much in terms of adherence.

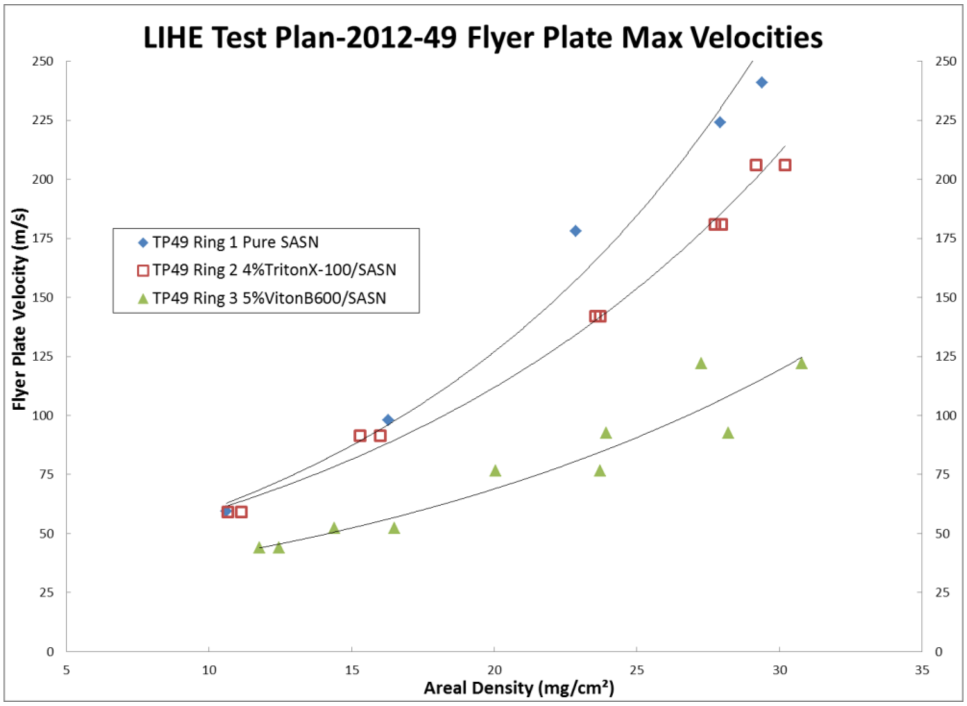

Figure 19, Maximum achieved flyer plate velocities with respect to the deposited amount of explosive.

Front-Surface Particle Velocity Measurements

All three FSPV diagnostic recordings were recovered with, but the signal-to-noise in the data was difficult to reduce and plot. The peak particle velocity from each explosive/window interaction was determined from SIHREN, a Sandia National Laboratories developed PDV reduction program [23]. Figures 20, 22, and 23 displays the data collected for the FSPV diagnostic on each target ring. Only the first incident shock wave in the PMMA window was considered and everything after that was a shock wave reflection from the opposite face of the window and spall after about 2-μs due to lack of light returns as seen in Figs. 20 and 22. Spall was seen in Ring 1 and Ring 2, pure SASN and assumed to occur in the surfactant altered SASN as evidenced in Figs. 20 and 21. The window for Ring 2 was not recovered from the test since the window was not found inside the large test cell. The Viton doped SASN was not sufficiently strong enough to spall the window as evidenced by the condition the recovered window in Fig. 24.

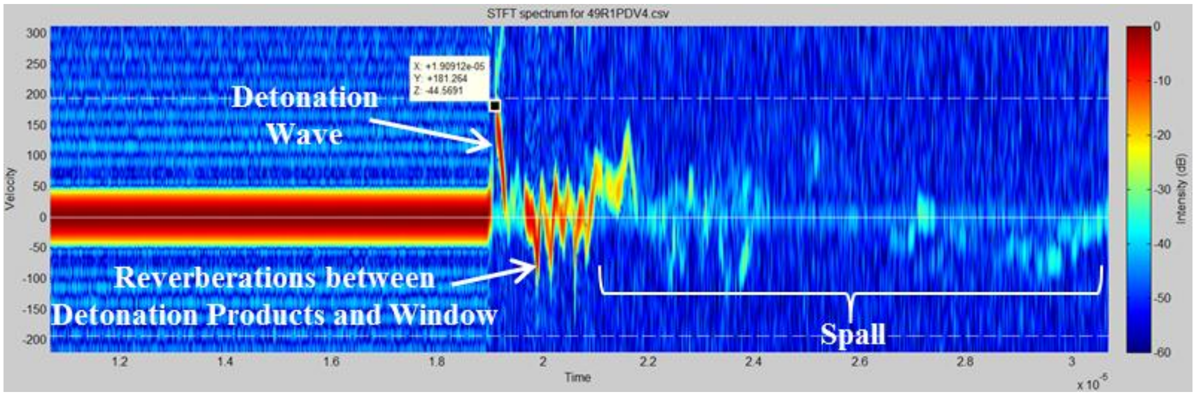

Figure 20, Particle velocity profile for FSPV of pure SASN with peak particle velocity and peak TOA labeled. The first spall is suspected to occur after the rear window face reflected shock wave is traveling back to the spectrally coated face. When the shock wave reflects once again, another spall plane near the spectrally coated surface is formed. Light immediately drops because of the two spall planes scatter the laser light. Reverberations in this case are the reflected shocks from the detonation products and window rarefactions. Velocity is in meters per second and time is in seconds x 10^{-5}.

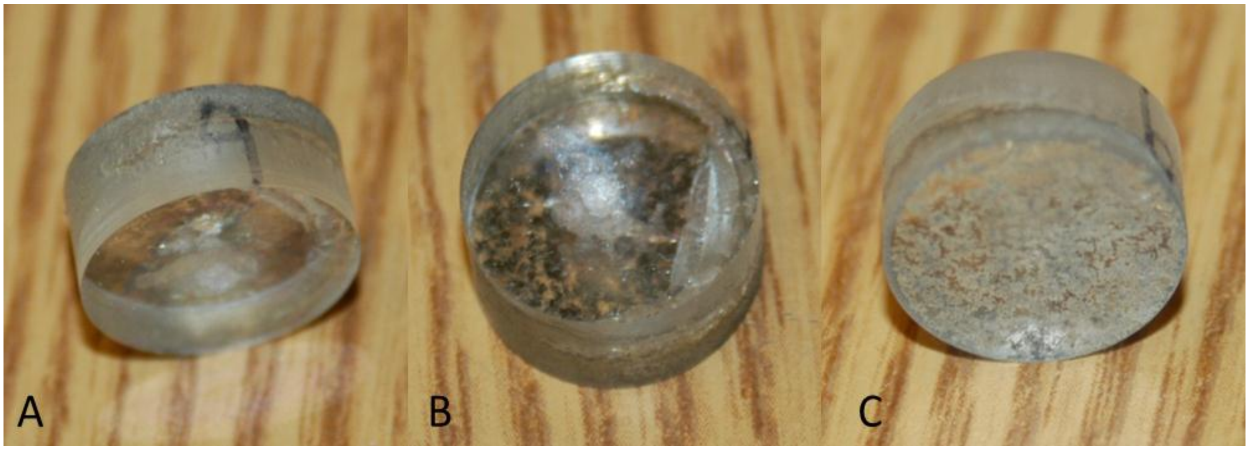

Figure 21, PMMA window recovered from Ring 1, pure SASN. Spall planes are seen in photos A and B near front and rear. Detonation pattern was left behind on surface in photos B and C as well as some spectral coating remained.

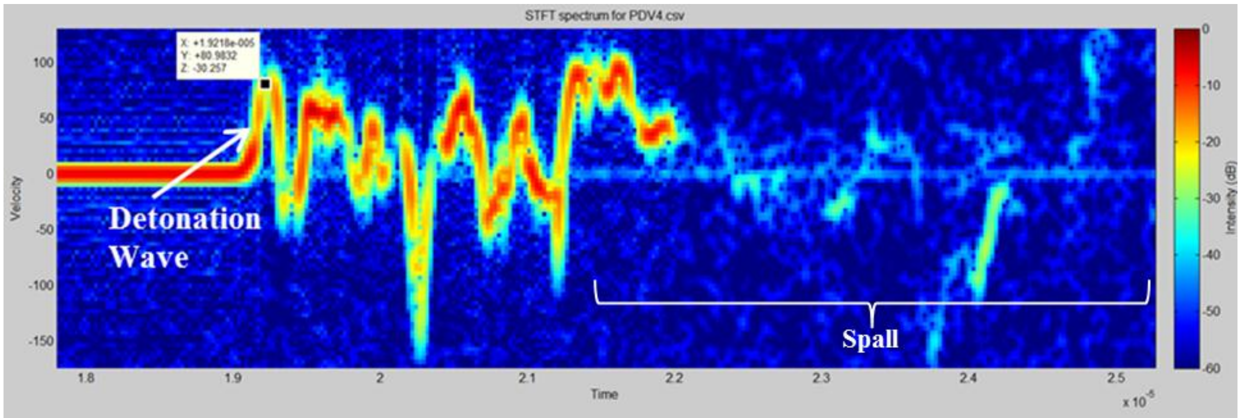

Figure 22, Particle velocity profile for FSPV of 4% Triton X-100/SASN with peak particle velocity and peak TOA labeled. Velocity is in meters per second and time is in seconds x 10^{-5}.

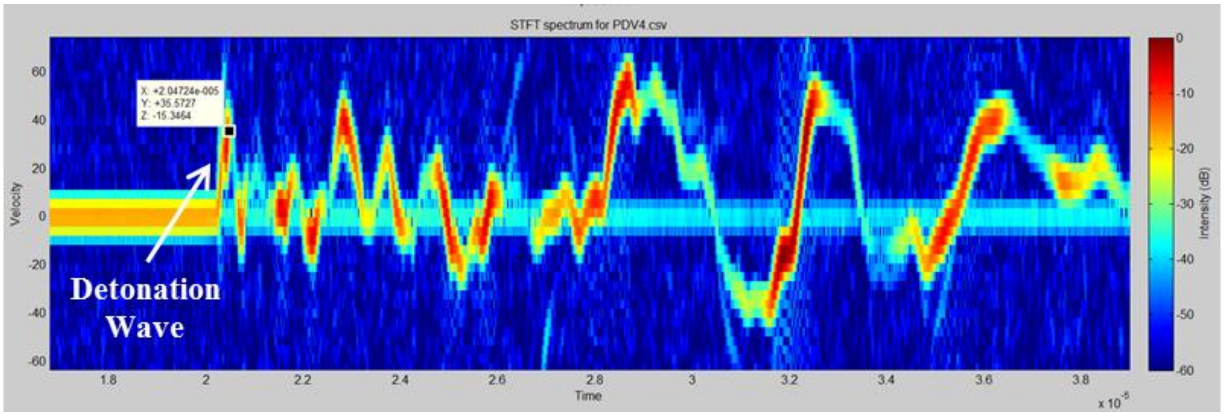

Figure 23, Particle velocity profile for FSPV of 5% Viton B600/SASN with peak particle velocity and peak TOA labeled. Velocity is in meters per second and time is in seconds x 10^{-5}. No PMMA spall is evident either in this trace or on the recovered window specimen.

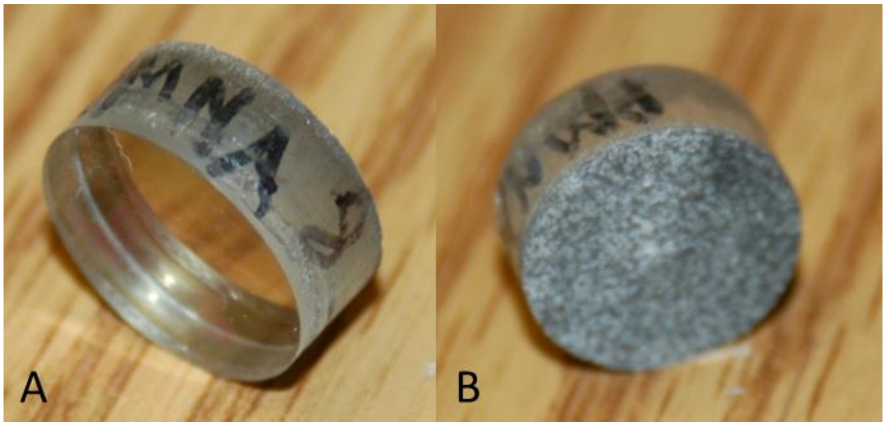

Figure 24, Photo A shows the rear surface of the PMMA window from the Viton doped SASN FSPV with no evidence of spalling of the window. Photo B shows the detonation pattern left on the spectrally coated surface.

The rough estimate of each pressure spike as measured using the Deal equation is shown below in Table 1. All three explosives had transitioned to a detonation state in less than the thickness reported in Table 1 based on the 10% to 90% rise time being always shorter than the full-width half max (FWHM) pulse width. The P_{spike}, rise time, and FWHM pulse width data are only rough estimates granted the particle velocity traces are difficult to reduce. Only the 5% Viton B600/SASN trace gave more accurate data for the P_{spike}, rise time, and FWHM pulse width because the entire trace was present and light did not "drop-out" as was the case for the other two explosives. The pure SASN was the most powerful LIHE produced in this shot series and agrees with ballistic pendulum and flyer velocity data. The Triton X-100 treated SASN was the next most powerful, which remaining explosive output diagnostics agree with this conclusion. The Viton B600 doped SASN had the least power, as hoped, and this was also found to agree with the rest of the explosive output diagnostics.

Table 1, Front-Surface Particle Velocity Transformed into P_{spike}

Explosive Type	Measured Average Probe-to-probe Detonation Velocity (mm/μs)	Average Thickness of LIHE (μm)	Standard Deviation of LIHE Thickness (μm)	Measured Density (g/cc)	Standard Deviation of Measured Density (g/cc)	Calculated P_{spike} from Deal Equation (Kbar)	10% to 90% Rise Time (μs)	FWHM (μs)
SASN	0.308	489.9	18.2	0.540	0.024	3.12	0.1	0.17
4% Triton X-100/SASN	0.312	530.2	27.5	0.541	0.033	1.35	0.1	0.15
5% Viton B600/SASN	0.114	518.2	26.3	0.544	0.032	0.51	0.1	0.29

Embedded Fiber Optics Measurements

All three EFO rosettes returned valuable and new data concerning the deflagration/detonation velocity as well as pulse shape, which indicates when and where DDT occurs in the explosive. However, not all probes returned easily interpretable data for various reasons to be discussed in following paragraphs. The diagnostic had a very helpful timing fiducial for each probe that allowed each probe to be a stand-alone TOA diagnostic, but data is inconsistent with the traditional method of pin-to-pin TOA determination since complex shock and detonation phenomena are occurring. Figures 27-29 display the recorded traces and display the special timing fiducial as well as the DDT characteristics of each explosive. The special timing fiducial was confirmed by CTH analysis with a simple two-dimensional configuration of arbitrary SASN modeled by the Jones-Wilkens-Lee approximation, two EFO fibers, and a drilled-out aluminum substrate that mocked the typical geometries seen in all three explosive tests. The explosive model did not account for DDT and build-up of detonation since a future model will be based on the data collected from EFO and FSPV measurements. Figures 25 and 26 below show the results from the model and the ability of the model to give an explanation of the second particle velocity jump that is seen in Figs. 27-29 in some instances. However, there are some unexplained inverted surface reflection timing fiducials seen in Figs. 28 and 29. Another twist to this data and second particle velocity jump is that a previous study pointed to whether or not a rearward traveling detonation, or retonation, could be occurring and cause the second particle velocity jump seen in the Figs. 27-29 [1].

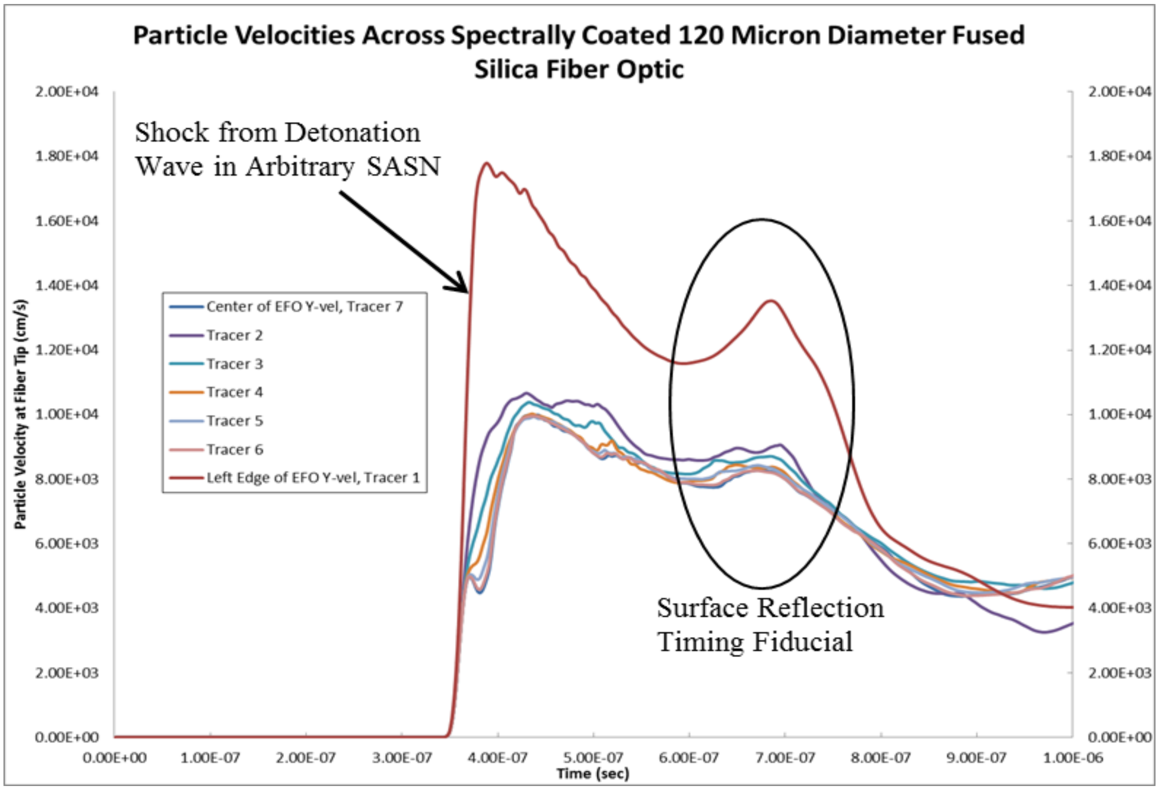

Figure 25, Two-dimensional CTH modeling results for arbitrary SASN detonation wave impacting an EFO tip and reflecting off the aluminum substrate.

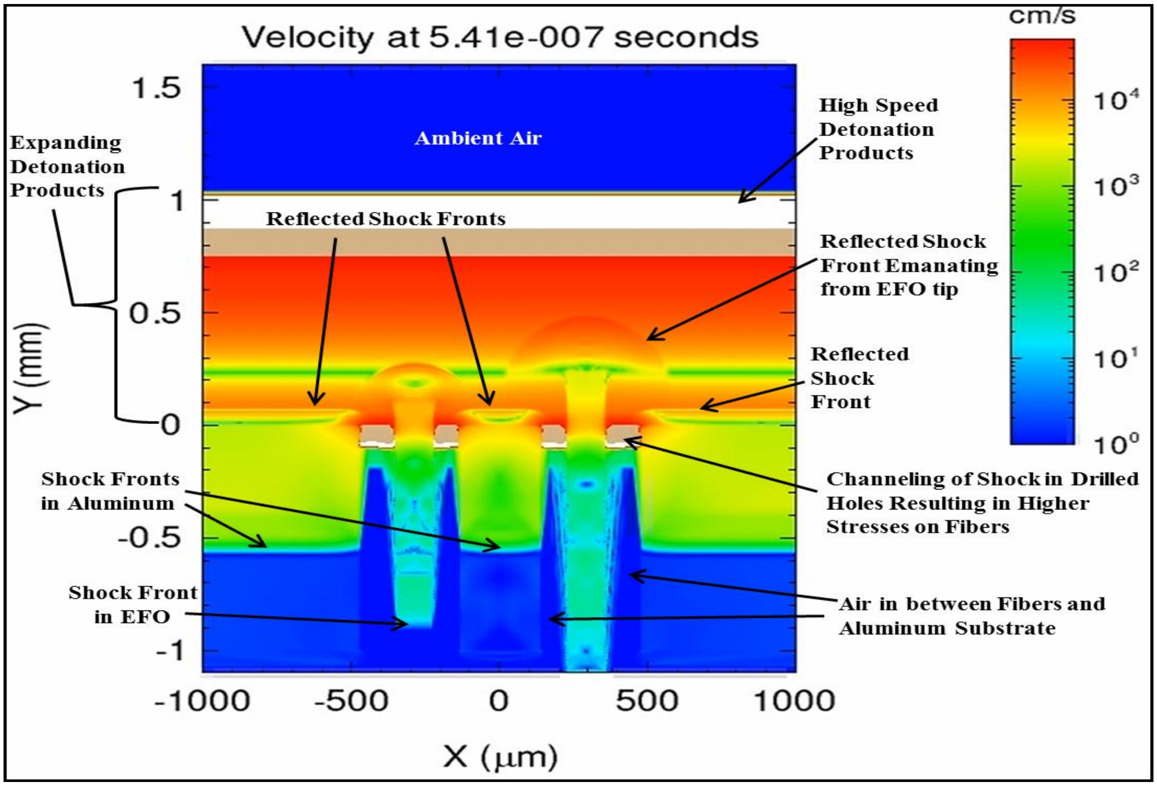

Figure 26, Image from two-dimensional CTH simulation of two EFOs in a typical experimental geometry seen in TP49. The tallest EFO is at an elevation of 254-μm and the shorter one is at 127-μm. This is very similar to Fig. 12 arrangement of EFOs.

Table 2 below documents the characteristics of each explosive giving a definition for what is considered a deflagration wave or a detonation wave based on rise time in comparison to the pulse width as was used for FSPV. Probes PDV6, 7, and 8 from Ring 3, the Viton doped SASN, had questionable deflagration waves to interpret as best seen in Fig. 29. The DDT transition occurred in a distance less than the average thickness of LIHE recorded in Table 1, but more detail is provided as to which two probes the DDT phenomena occurred between. Inspection of Table 1 gives the reason why Rings 1 and 3 probes PDV8 on each did not give any data with respect to TOA of the deflagration wave. The probes were simply sticking outside of the explosive layer and therefore could not detect any compression wave generated from inside the explosive. However, any compression wave detected prior to the surface reflected shock is from the shock generated at the LIHE/air interface. Proper reduction of this air blast data would reveal the air shock pressure prior to and potentially after the one-dimensional Mach formation from the combination of the air shock and the reflected surface shock.

Figure 30 is a distance-time (X-T) plot that plots the half max TOA values for each reducable EFO probe embedded in the explosive and the relative location from the explosive/air surface. The slopes of these lines are the reported detonation velocities for SASN, 4% Triton X-100/SASN, and 5% Viton B600/SASN as seen previously in Table 1. There is a delay in each explosive for the ignition time, which is defined as the first probe to detect the deflagration wave. The light array emits photons at approximately 5 to 8-μs and the induction time (time from first energy deposition to explosive ignition) is approximately 10 to 13-μs.

The measured fiber tip particle velocity time-history is indicative of the detonation-induced shock strength, Taylor wave rarefaction effects, and the shock-induced change in refraction. Assuming no retonation, the particle velocity trace continues as the combustion products are still under pressure and expand, but the velocity changes as the reflected shock from the surface sweeps back up the fiber. As the reflected shock propagates through expanding and probably still chemically condensing detonation products, a second particle velocity jump is induced as seen in Figs. 27-29. However, the TOAs of each pin do not make sense in terms of when each pin should be re-shocked because the TOA for the pin closest to the reflected surface detects a particle velocity jump last and the farthest away pin detects a particle velocity jump the earliest. The reflected shock seems to be increasing in velocity, which is contrary to shocks propagating in a medium unless multiple shocks are coalescing. Another theory is that a rearward propagating detonation, or retonation, is occurring in the compacted and partially reacted explosive and is accelerating [1]. Figure 31 is a plot of the pin-to-pin velocities that reveals information about the state of the expanding combustion products or potentially a retonation wave velocity from each explosive tested. This was unprecedented data that was measured and is extremely important for future model modifications to the LIHE for hydrocode simulations. The initial velocities (at ~120-µm above surface) in Fig. 31 agree very well between the two methods employed to measure the wave propagation and only the Viton measurements are inconsistent.

Table 2, Peak Rise Time, Full-Width Half Max Pressure Pulse Width, and Wave Type

Ring # and Probe #	Distance from Aluminum Surface (µm)	Probe Distance From Explosive Surface (µm)	Standard Deviation of Probe Distance from Explosive Surface (µm)	10% to 90% Peak Rise Time (µs)	FWHM Pulse Width (µs)	Deflagration or Detonation Wave
R1,PDV5	119.4	370.5	18.2	0.2619	0.3372	Detonation
R1,PDV6	257.8	232.1		0.6273	0.5256	Deflagration
R1,PDV7	381.0	108.9		1.614	1.126	Deflagration
R1,PDV8	509.3	-19.4		N/A	N/A	N/A
R2,PDV5	123.2	452.1	46.4	0.0888	0.2214	Detonation
R2,PDV6	252.7	322.6		0.0858	0.3471	Detonation
R2,PDV7	389.9	185.4		0.7497	1.163	Detonation
R2,PDV8	522.0	53.3		0.8655	0.5976	Deflagration
R3,PDV5	128.3	344.1	36.4	0.1737	0.4644	Detonation
R3,PDV6	259.1	213.3		N/A	N/A	Deflagration
R3,PDV7	381.0	91.4		N/A	N/A	Deflagration
R3,PDV8	518.2	-45.8		N/A	N/A	N/A

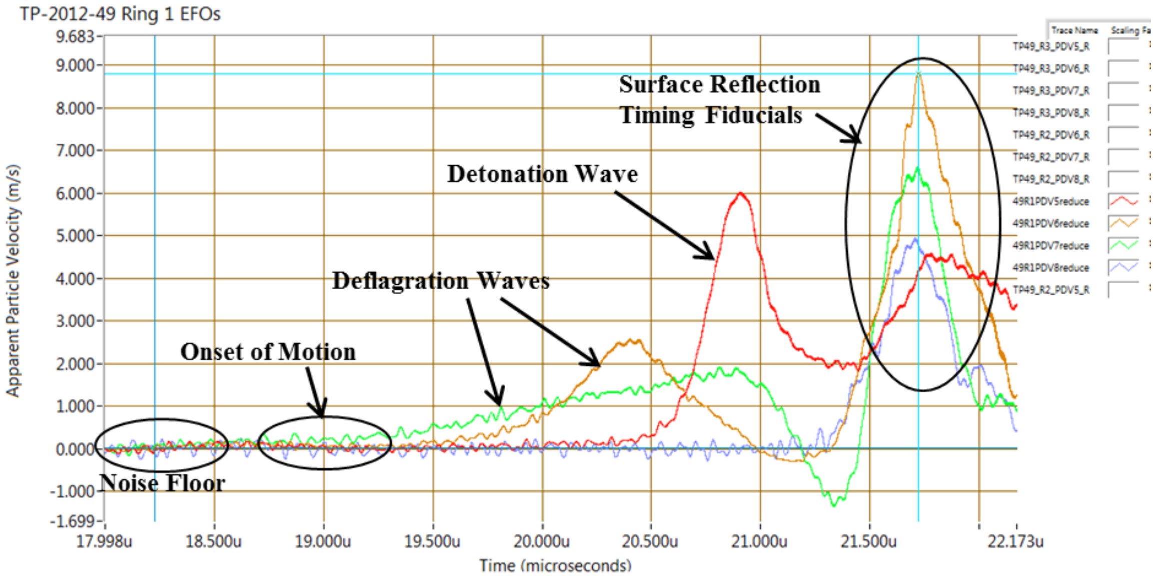

Figure 27, Apparent particle velocity traces from EFOs in the unaltered SASN explosive ignited from the exposed outer surface by high intensity visible and ultraviolet light. Notice trace PDV8 (light purple) only has the suspected surface reflection timing fiducial and no other data visible before this wave.

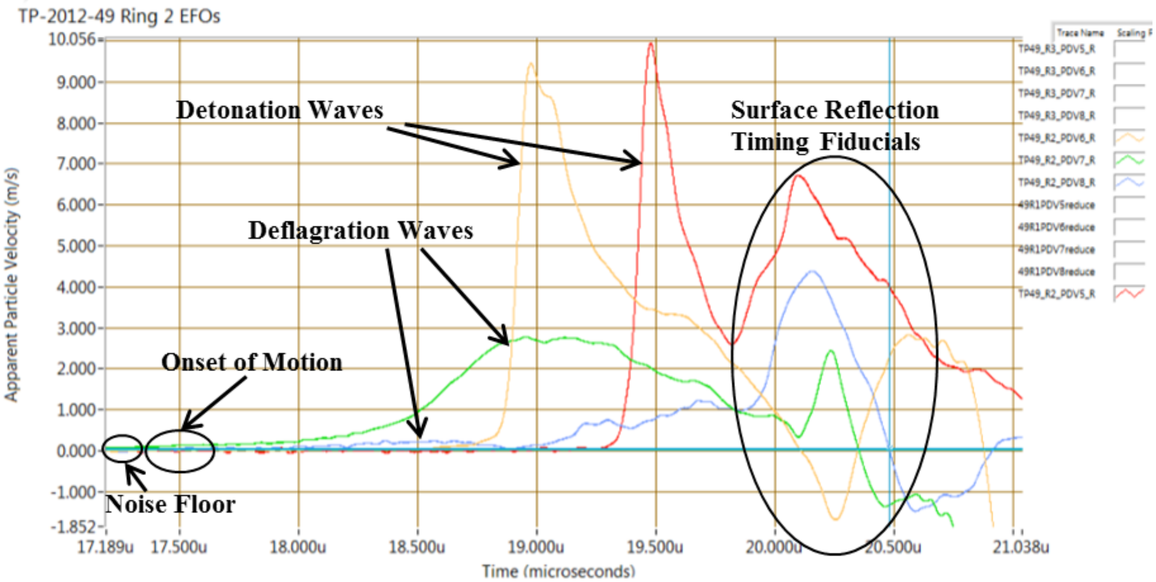

Figure 28, Apparent particle velocity traces from EFOs in the 4% Triton X-100/SASN explosive ignited from the exposed outer surface by high intensity visible and ultraviolet light. Notice the PDV6 trace has a negative particle velocity for the suspected surface reflection timing fiducial.

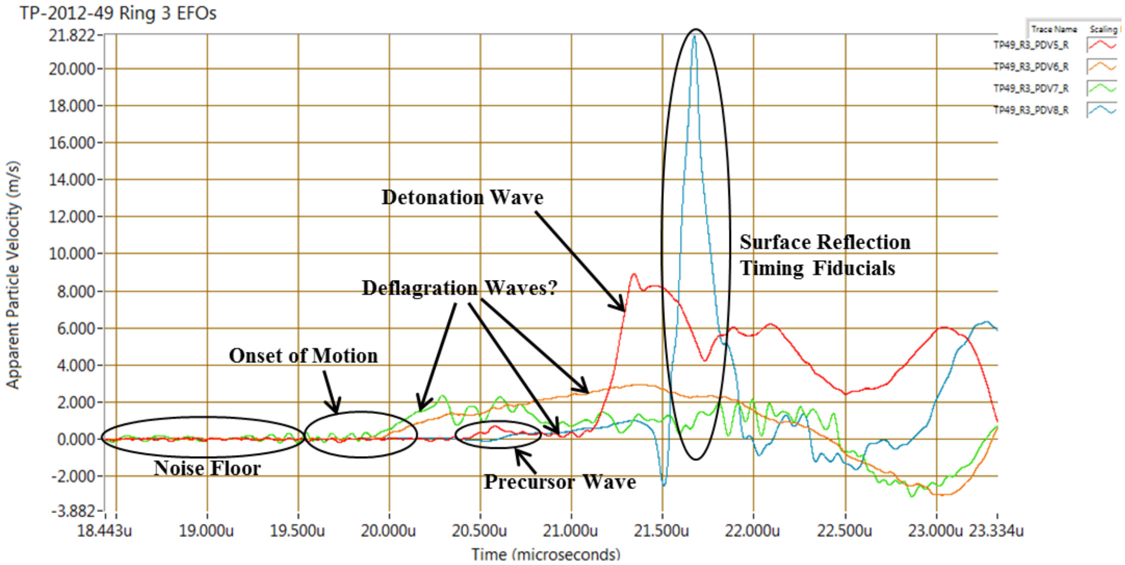

Figure 29, Apparent particle velocity traces from EFOs in the 5% Viton B600/SASN explosive ignited from the exposed outer surface by high intensity visible and ultraviolet light. Notice traces PDV 7 (green) and PDV6 (tan) are missing the distinguishable and suspected surface reflection timing fiducials. Notice the inverted suspected surface reflection timing fiducial for the trace of EFO5 (red).

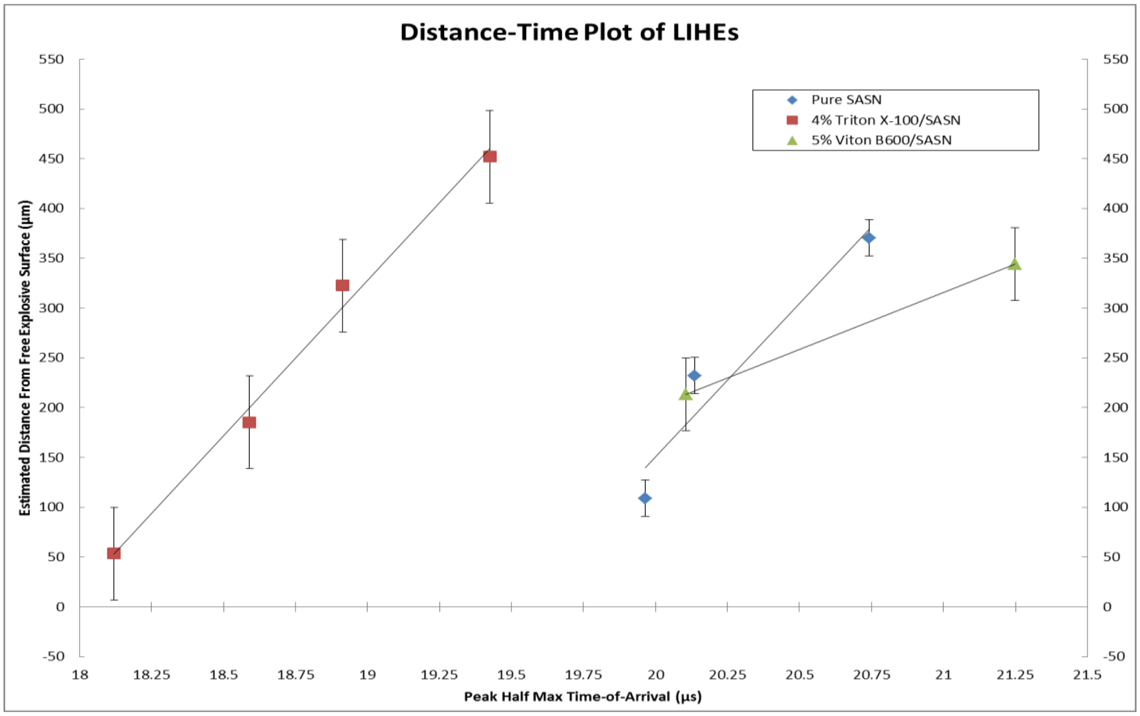

Figure 30, X-T plots for the EFOs from each explosive mix tested giving the first true detonation wave velocities through the thickness of thin spray-deposited explosive when the exposed outer surface is light initiated. The slope of each line is the average deflagration/detonation velocity for that particular explosive and is listed in Table 1. Error bars are deduced from the adjacent coupon thickness measurements and are listed in Table 2.

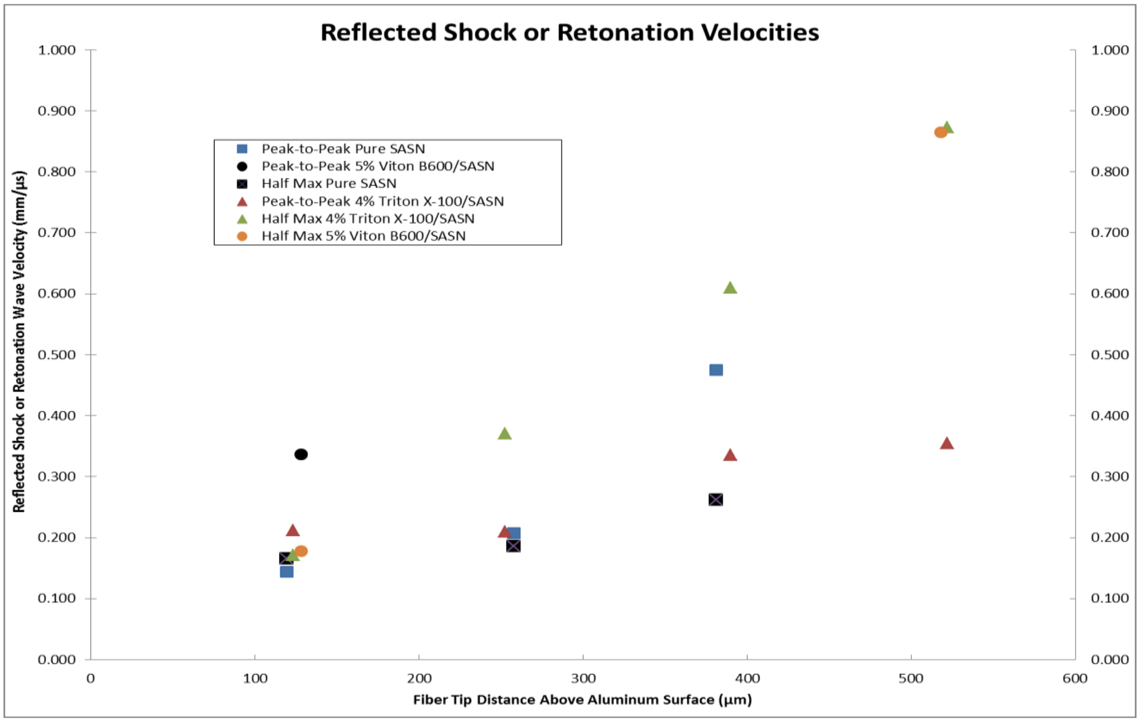

Figure 31, Plot of the suspected reflected shock or retonation waves in each LIHE. Displayed are two methods for determining the wave propagation velocity through the either expanding detonation products or retonation through compacted HE. Fiber tips are assumed to have not traveled far from their original positions due to the detonation and retonation and/or subsequent reflected shock.

Ballistic Pendulum Measurements

The control batch of pure SASN was calculated to be 109% of the nominal SASN specific impulse that is typically produced at the LIHE facility. This is slightly more powerful than the nominal explosive produced, but this is within the scatter seen from batch to batch. The 4% Triton X-100/SASN batch was 100% of the nominal SASN specific impulse, indicating no change due to Triton X-100 non-ionic surfactant. The 5% Viton B600/SASN batch was 76% of the nominal SASN specific impulse, which shows that 5% Viton B600 knocks down the impulse effectively. This last result was expected since addition of a phlegmatizer should decrease the power of an explosive. This last batch of composite explosive was made with the first batch of pure SASN, thus the impulse was knocked down by approximately 33% for areal densities above 15-mg/cm^2. Figure 32 displays the specific impulse data set from each LIHE produced for shot series TP49. "Stacking corrected" explosive performance refers to a correction needed to take into account the lateral losses around the perimeter of the explosive coupon when detonated to equate the specific impulse to a one-dimensional specific impulse [24].

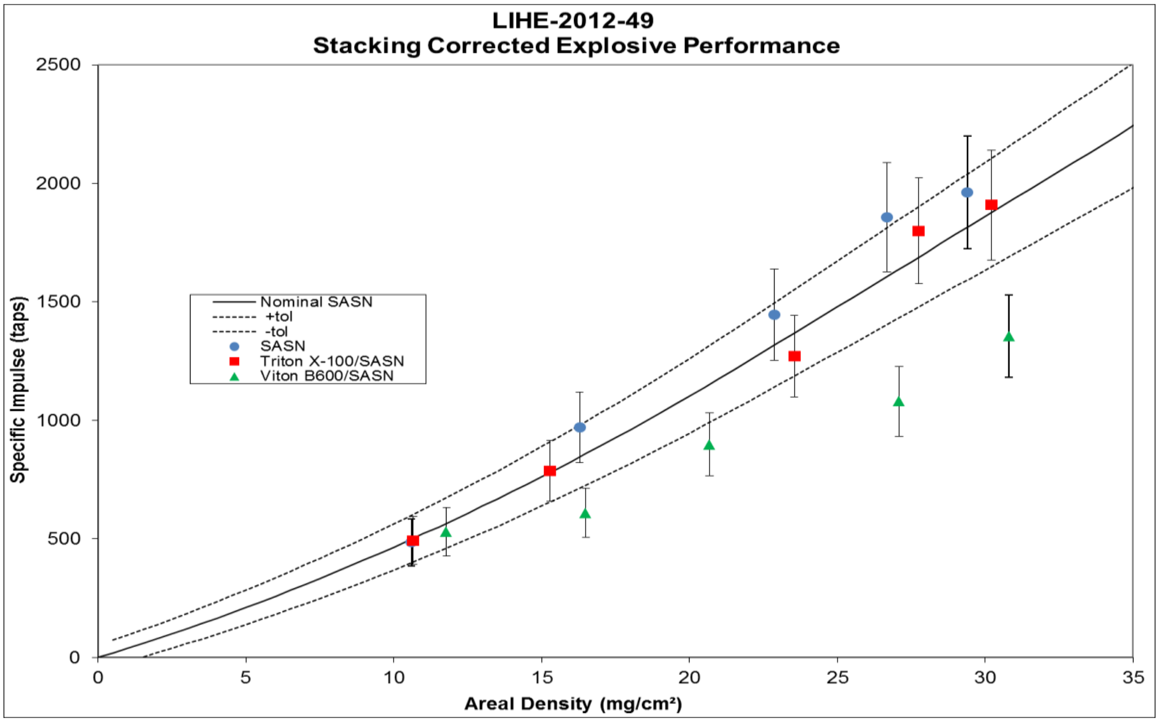

Figure 32, Output from ballistic pendulum for SASN and composite SASNs from each flyer plate test. Note that the pure SASN low areal density specific impulse is superimposed by the low areal density Triton X-100/SASN specific impulse data point. Error bars are a function of the measured specific impulse [24].

Averaged Bulk Density Measurements

Figure 31 displays the bulk density for each batch of LIHE produced in shot series TP49. The pure SASN batch was the easiest to measure and had the least uncertainty in the averaged bulk density as can be seen in the figure. There is a slightly distinguishable trend of increasing bulk density with increasing areal density that agrees with past data collected [1]. The increase in bulk density is caused by the spray process, when the impacting particles pack the porous explosive bed more and more efficiently. The bulk density variation in coupon to coupon and within a coupon results from samples exhibiting thickness changes. From the data, one can see that there is apparently no difference in the three batches of LIHE. The Triton X-100 non-ionic surfactant was thought to possibly change the density of the resulting explosive, but the data says otherwise. The technique is very difficult to perform granted the sprayed explosive is made of valleys and peaks thus introducing some relatively large error in some measurements as evidenced by the error bars.

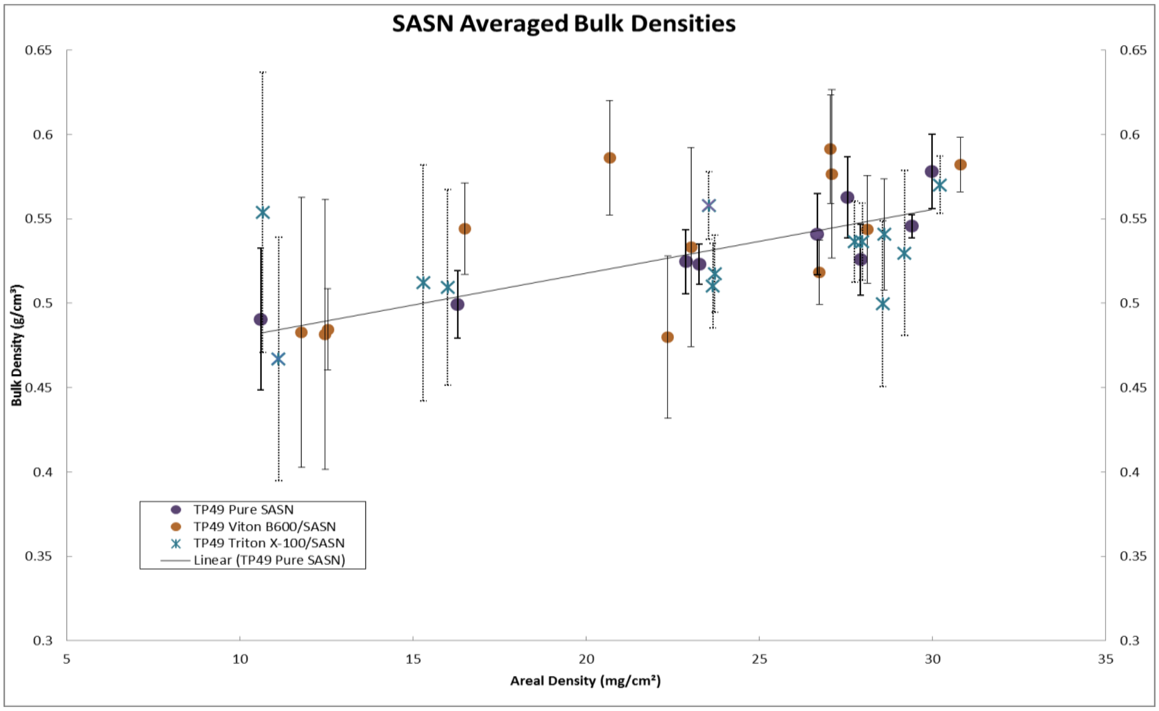

Figure 33, Average bulk densities of SASN as measured from Kovar coupons. Uncertainty bounds are attached on each data point and is an estimated standard deviation derived from the four measurements on a coupon perimeter.

SEM Images and Analysis

Figures 34-46 illustrate the complex structure of spray-deposited SASN and composite explosives as viewed through an FE-SEM. During ion-beam nano-tomography, three samples of the control batch SASN and the Triton X-100/SASN detonated. The final sample to initiate was a control batch, which initiated with a relatively slow ramp rate at 3kV [18]. Iridium coating prior to etching did not help with these samples, so the below images are from an earlier test series, TP48, and are similar to what was seen in SEM of loose powders from the current test series, TP49. Sadly, only the Viton B600/SASN sample survived the ion-etching and was analyzed across the full cross-section. The backscatter electron (BSE) images for each explosive are from deeper inside the particles and display differences in atomic number, or Z number. However, there was not a noticeable difference in the Z number throughout each matrix or between them as pointed out in Figs. 36, 39, and 42. A more definitive map of compositional difference with respect to the spatial location is best illustrated in Fig. 47. Early BSE analysis of pure SASN from shot series TP48 did show some compositional difference relative to spatial location, however many of the BSE images from that shot series also agreed with the ones collected from this study.

The two distinct matrixes, or phases, are present in this study as they were from the previous TP48 study (see Fig. 3 as compared to the below figures). Sintering is evident in Fig. 35, as was seen in the previous study [1]. In Fig. 38 some fibrous matrix is seen in an early stage of sintering, but the sintering that would occur from formulation and spraying may only exist with a liquid and driving force present (elevated temperature and flow current in beaker) [25]. Controlling the sintering and knowing exactly what factors are necessary for better matrix properties' control, which directly affect the explosive output. As the figures below suggest, the addition of Triton X-100 during formulation and Viton B600 after formulation did not control any matrix properties as thought. Figure 47 does show that Viton B600 constituents are within the matrix and well dispersed since the data was collected over a large portion of the sample as depicted in the following Fig. 48. All SEM images of the Viton doped SASN show that it is well dispersed since it is not an easy to distinguish phase from the others. More EDS maps of the other explosives would have been great additions, but the charging of the explosive samples prevented clear images from being produced.

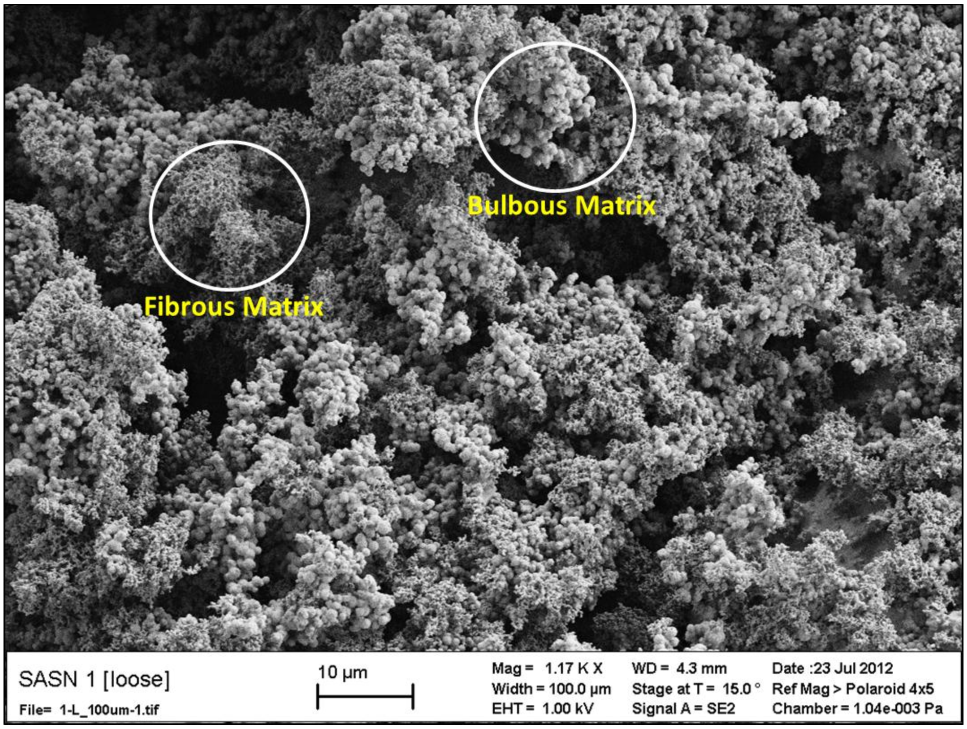

Figure 34, SEM image of pure SASN showing the structure of spay-deposited explosive matrix. Spray particles have agglomerated into the structure full of porosity and the same bulbous and fibrous structures seen from Fig. 3 from another SASN sample.

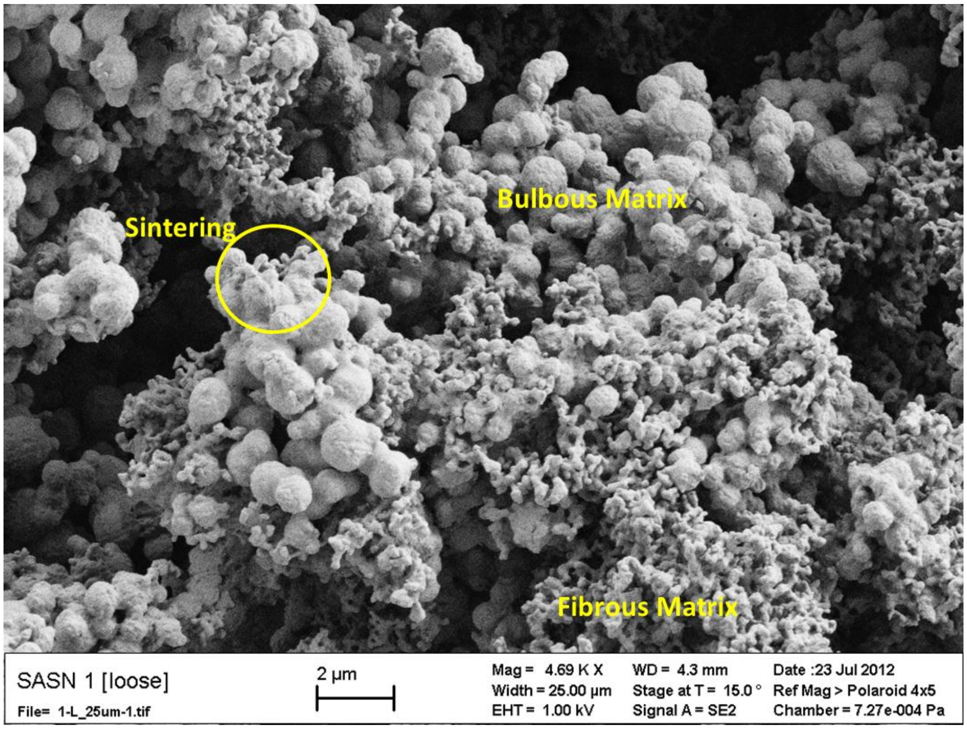

Figure 35, Fig. 34 zoomed in to observe the porous matrix of pure SASN. The fibrous phases appear to have sintered to the larger bulbous phases as seen and proposed in previous studies [1].

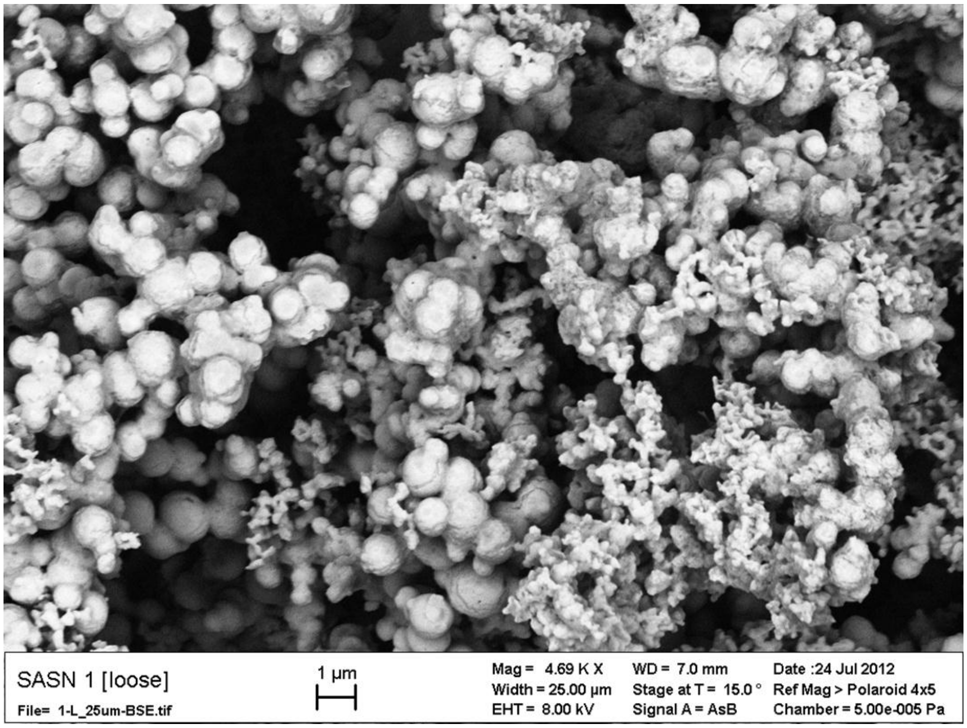

Figure 36, Backscatter electron (BSE) image from the pure SASN sample indicating the homogeneity of high Z numbered elements, namely silver. This adds credibility to the idea that there are not considerable differences in composition of either of the two different phases or matrixes.

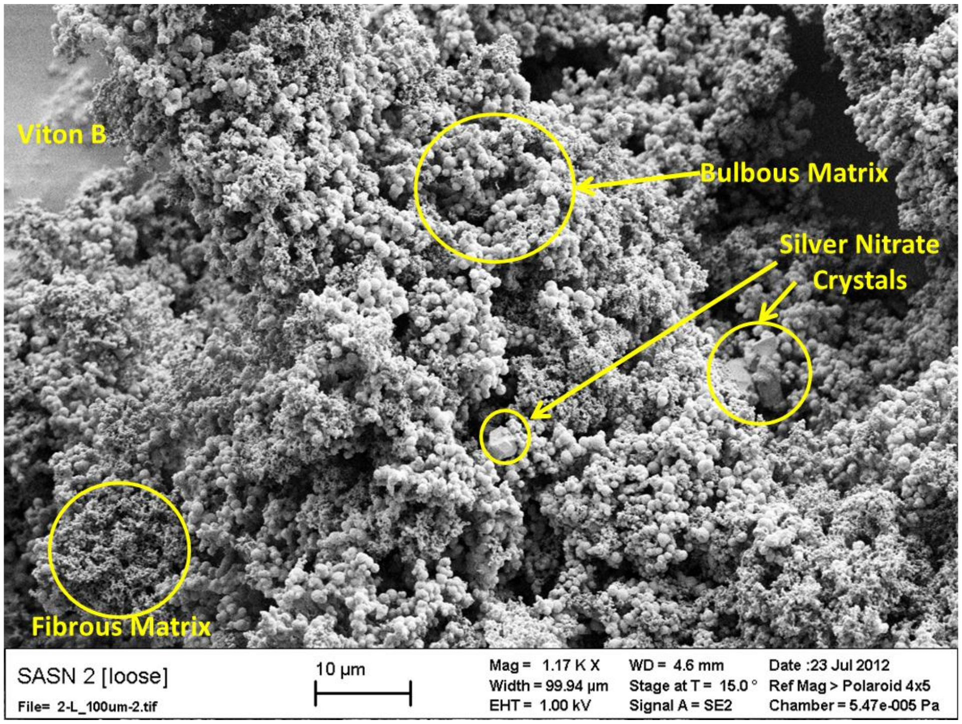

Figure 37, The Triton treated SASN appears exactly as the pure SASN sample. This particular sample had silver nitrate crystals apparent as was the case with pure SASN in shot series TP48. These crystals are not highly concentrated in the area of this image or elsewhere on the sample, which was also the case in TP48.

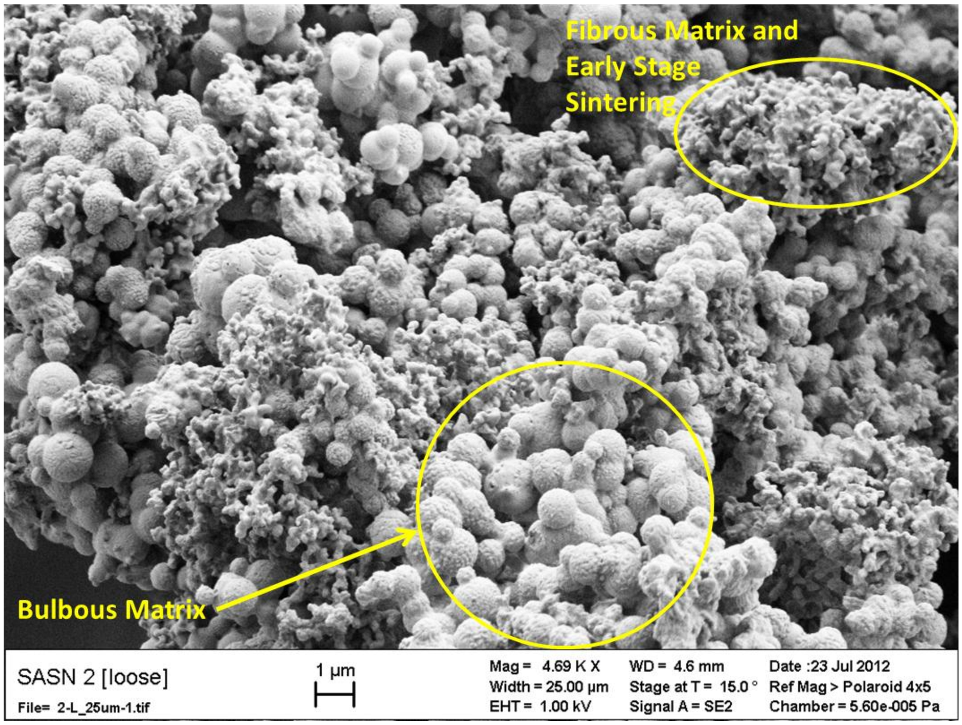

Figure 38, Close-up of Fig. 37 Triton X-100 treated SASN showing the distinct particles and phases created during formulation and spraying. Some fibrous matrix is seen in an early stage of sintering, but the sintering that would occur from formulation and spraying may only exist with a liquid and driving forces present [25].

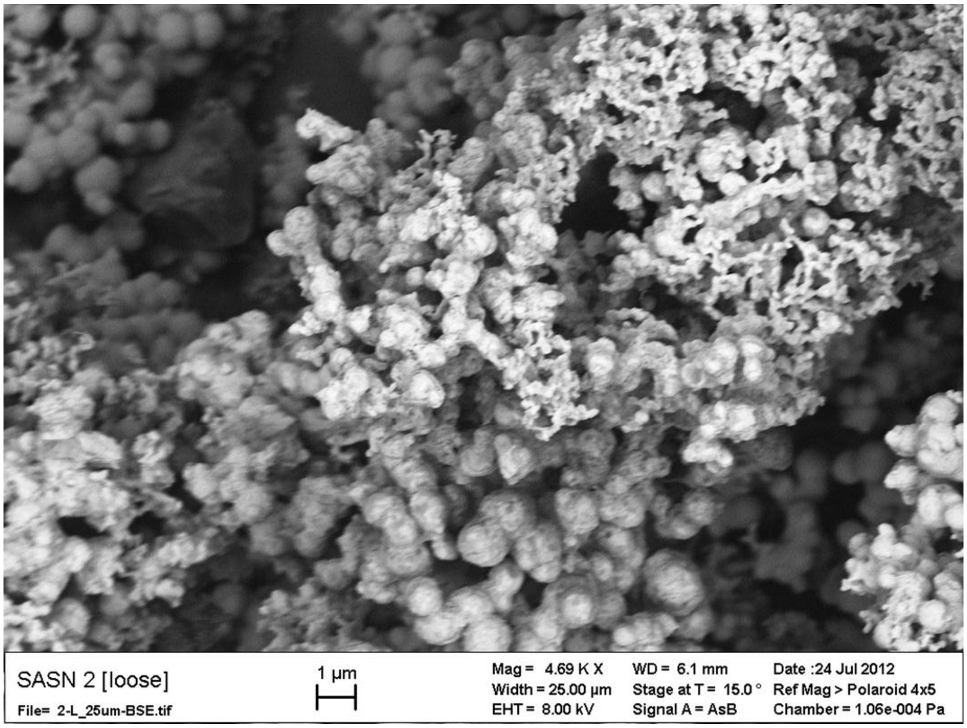

Figure 39, BSE image of the Triton treated SASN, again showing the homogeneity of the structures in terms of elemental composition.

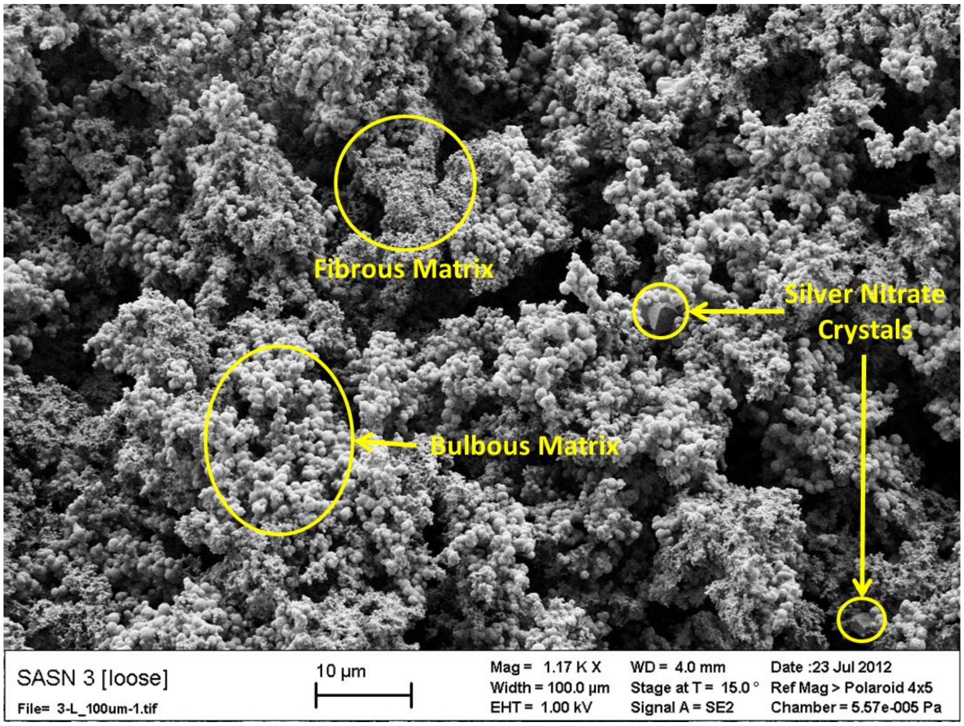

Figure 40, SEM image of Viton B600 doped SASN showing the same features from pure and Triton treated SASN.

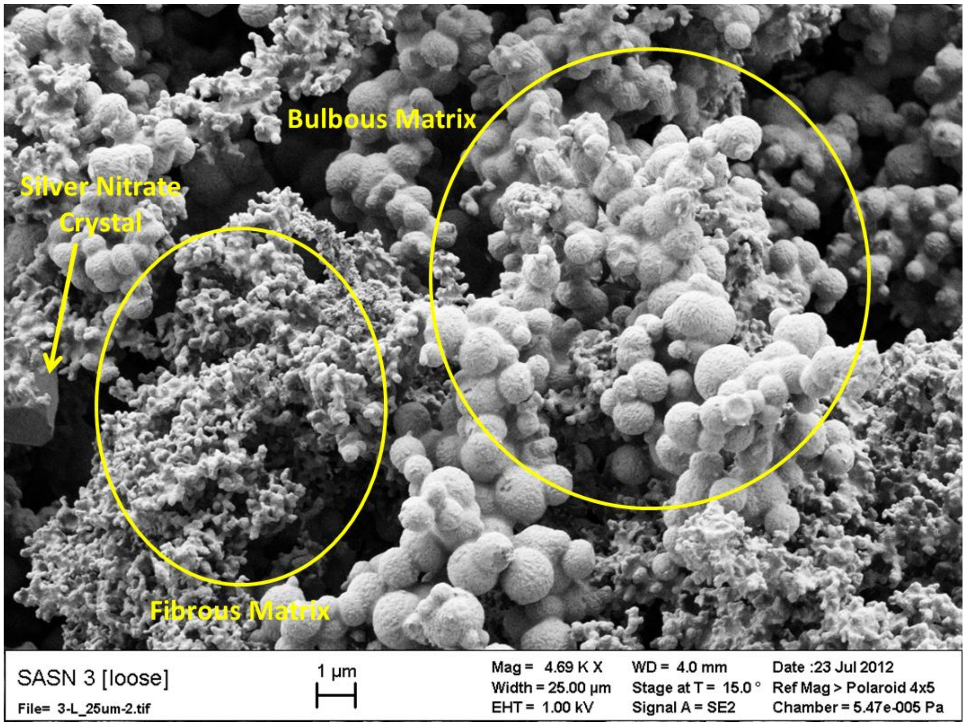

Figure 41, Close-up SEM image of Fig. 40 showing the details and the topography of the Viton doped SASN.

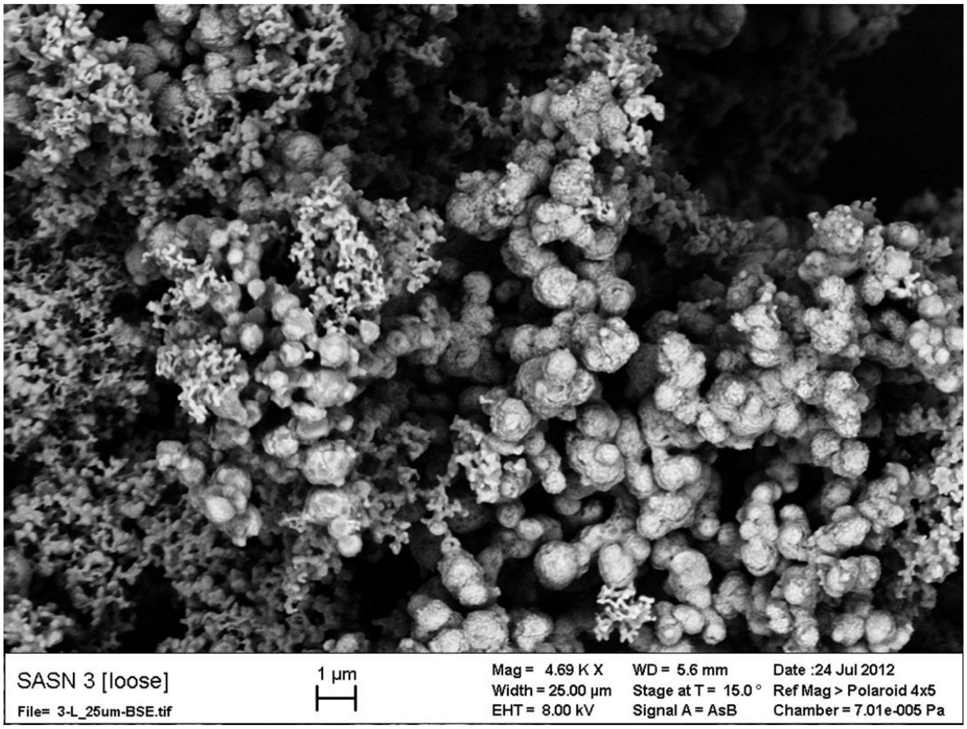

Figure 42, BSE image of the Viton doped SASN sample once again showing the homogeneity of the silver within the two structures.

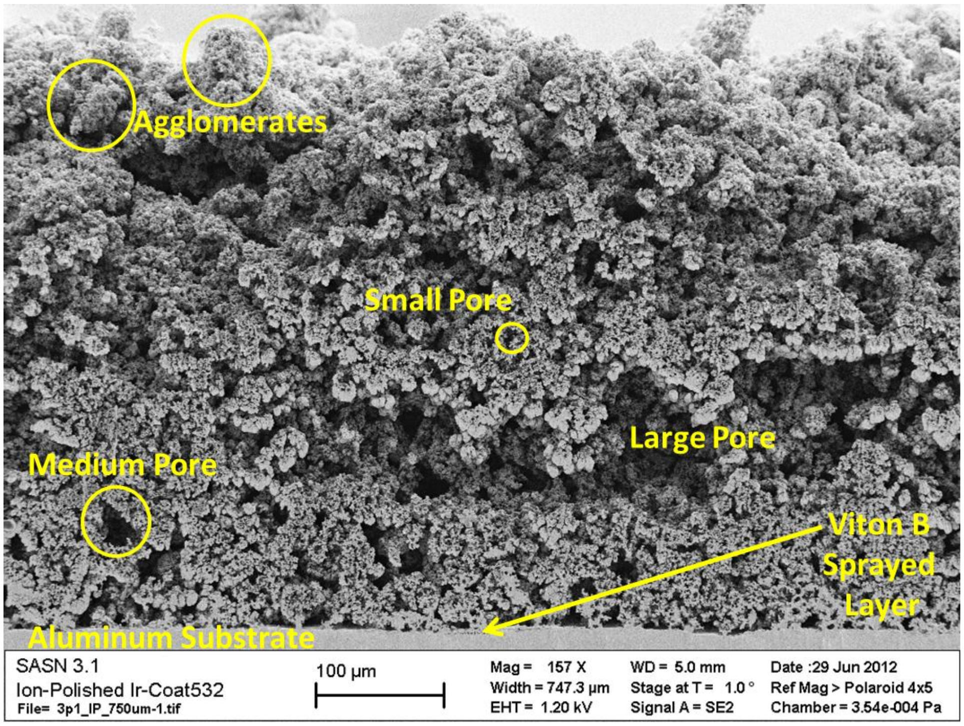

Figure 43, SEM image of ion-polished Viton B600/SASN which shows the same structures seen in a previous study [1]. The large pores can extend over hundreds of microns as can be seen in the above image. Medium pores are about the same size as most of the agglomerates, <100-µm. Small pores are on the same order of size as the bulbous and fibrous grains.

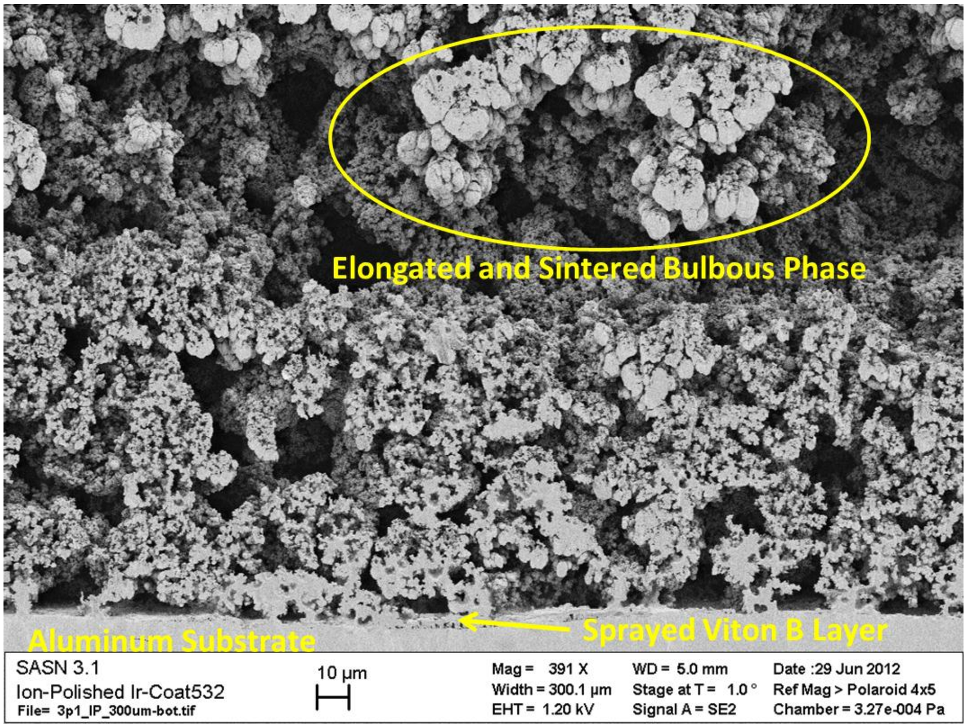

Figure 44, A close-up of the previous SEM image better detailing the explosive spray paint adhered to the Viton B and aluminum substrate. Some of the bulbous matrix is less spherical as normally seen and more sintered as was seen in shot series TP48.

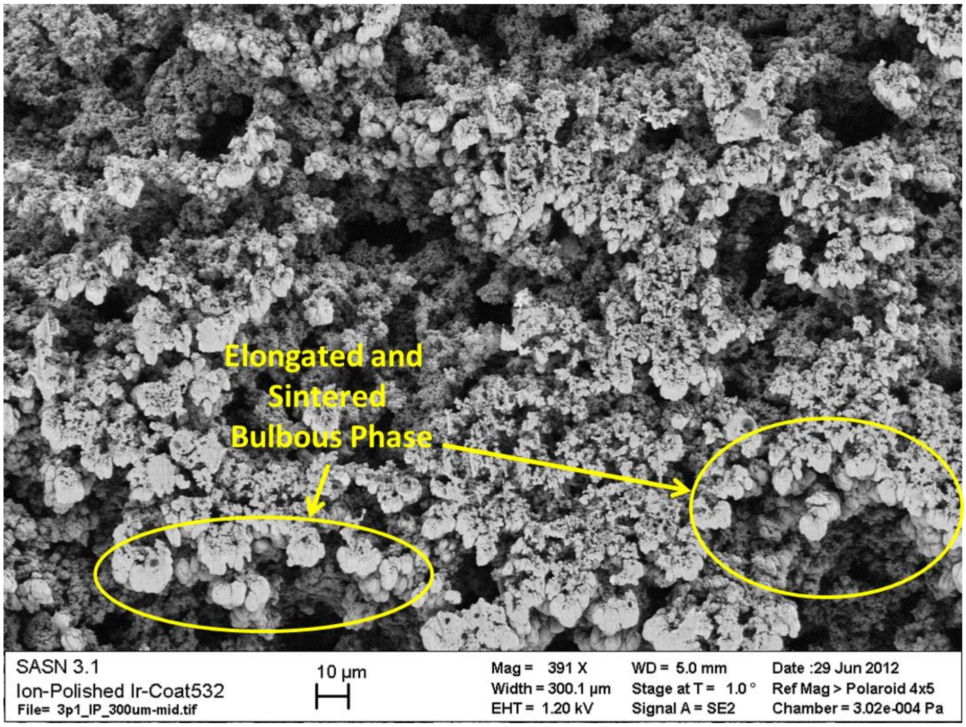

Figure 45, SEM image of ion-polished Viton B600/SASN Fig. 43 showing more detail in the mid-section.

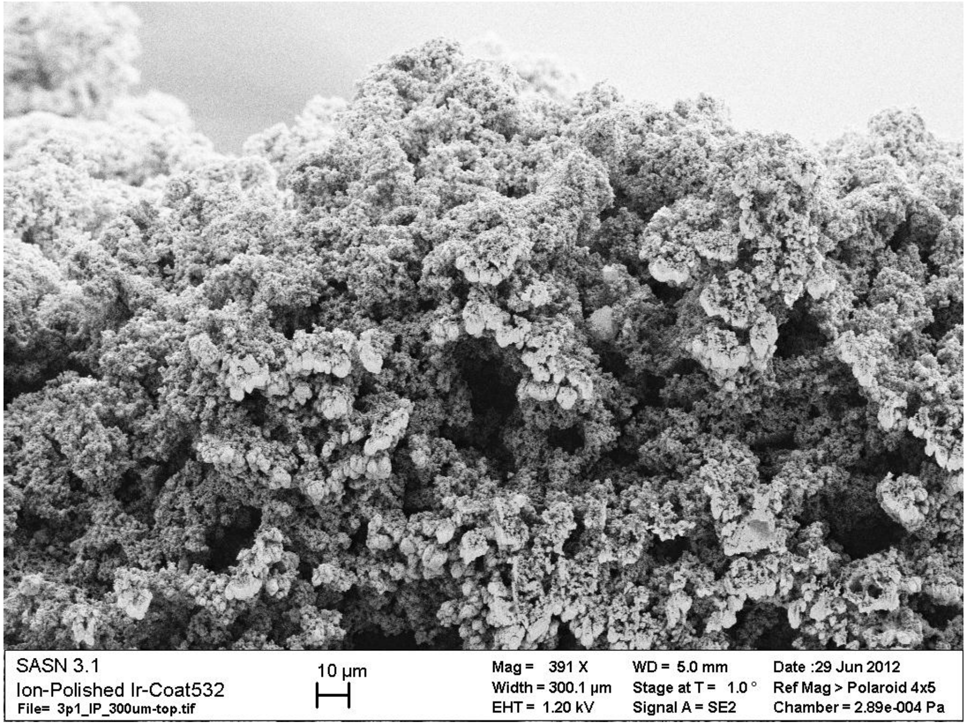

Figure 46, SEM image of ion-polished Viton B600/SASN Fig. 43 showing more detail in the top-section and surface. The same structures are seen throughout the matrix as was the case in shot series TP48, which was pure SASN.

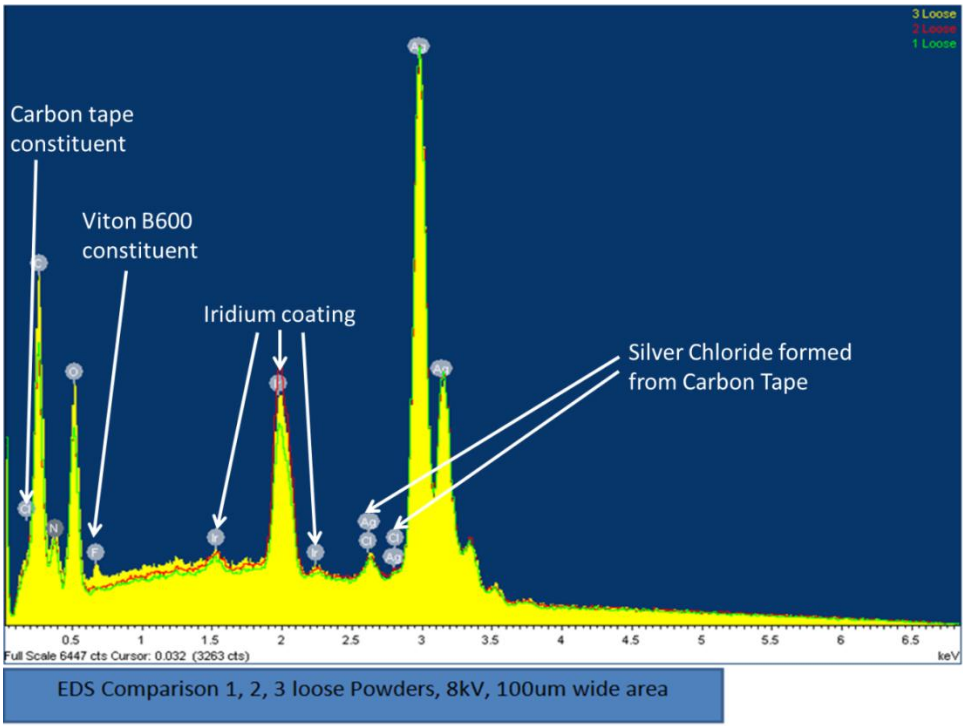

Figure 47, Energy-dispersive X-ray spectroscopy output for elements and compounds in pure SASN (labeled 1 Loose in green), 4% Triton X-100/SASN (labeled 2 Loose in red), and 5% Viton B600/SASN (labeled 3 Loose in yellow). The silver chloride formed was determined to be formed from reaction with the conductive carbon tape used to mount the samples on [18].

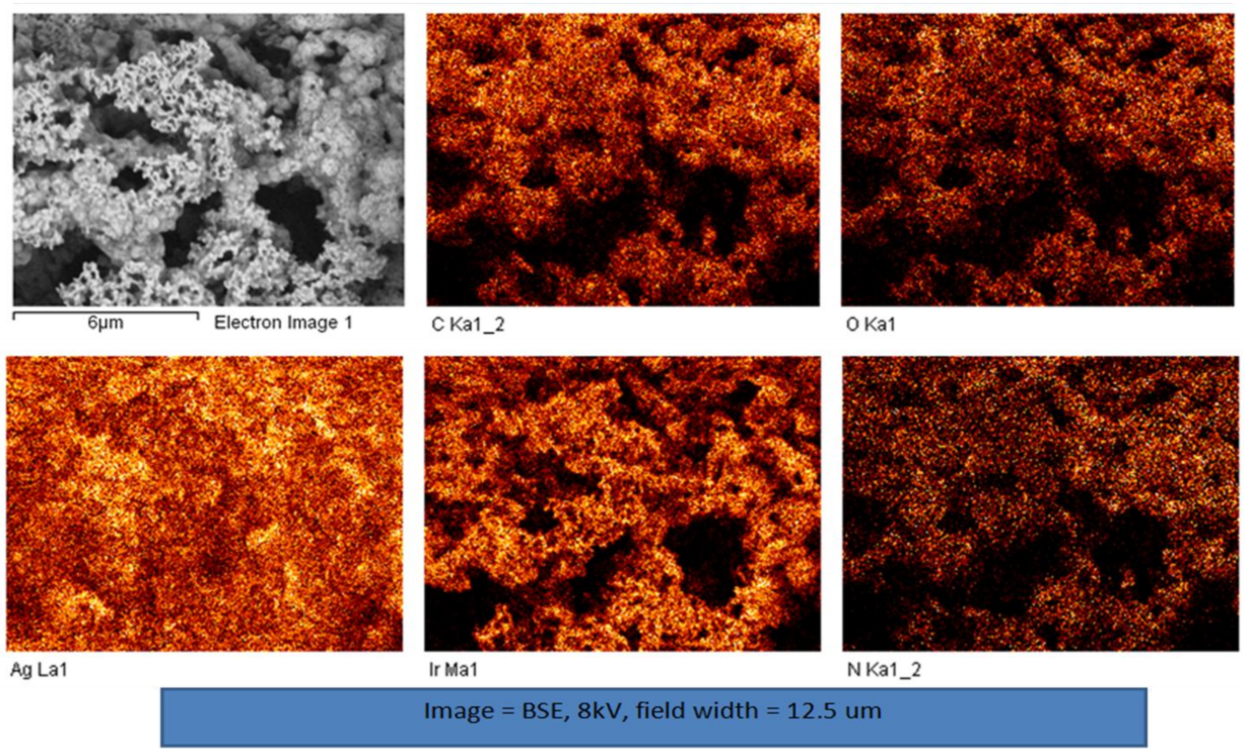

Figure 48, The upper left image is a BSE image of the sample used to produce the following EDS maps for SASN. The samples charged even though an iridium coating was physically vapor deposited onto the surface, causing most images to appear out of focus. These were the most decent EDS maps for Viton B600/SASN [18].

Vibrational Spectroscopy Analysis

The IR spectra from each sample are shown below in Figs. 50, 52, and 54 with corresponding maps to where each spectrum was taken from spatially on each sample in Figs. 49, 51, and 53. The extent of heterogeneity was determined with the two vibrational spectroscopy analyses and shows that there is mostly homogeneity in all three explosives formulated, except some minor variation as seen in Fig. 50. Data collected on all pure SASN and SASN composites agreed well with pure SASN investigated from TP48. Interestingly enough, TP48 data was compared to silver acetylide and silver nitrate references and found some disagreement, which is also the case for TP49 vibrational spectra and to be expected for a molecule of silver acetylide bonded to silver nitrate. Alam [22] points out in her study of the pure SASN material that the right plot presented in Fig. 50 shows the silver acetylene band at 3423-cm^{-1} may be due to water since the reference is collected when wetted. The band at 1813-cm^{-1} is thought to be the carbon to carbon double bond that is seen very strongly in Raman spectra in Figs. 55-57. However, since reference samples are collected in water, the bands reported in this study for pure SASN may be shifted in wavenumber to the reported 2069-cm^{-1} [26]. Infrared bands 1752-cm^{-1} and 1742-cm^{-1} might be a carbonyl, or carbon to oxygen double bond, but there is not much of this type of molecule present as pointed out in the below IR data due to the low absorbance. The 722-cm^{-1}, and 711-cm^{-1} are thought to be a silver carbon stretching, but this doublet may also be strictly from hydrocarbons [27]. The Raman band at 1040-cm^{-1} was determined to be from the nitrate symmetric vibration [26].

The Triton X-100 treated SASN was interesting because both IR and Raman report not a single band to compare to the literature [22]. In short, the Triton X-100 non-ionic surfactant was washed out or possibly destroyed by the nitric acid production during formulation then washed out via the washing process. Essentially the Triton X-100/SASN was pure SASN with the nominal explosive output. The Viton B600 doped SASN was consistent with pure SASN data, but included a few extra bands that correspond very nicely to the Viton B reference as can be seen in Fig. 54. Note that the Viton B600 will have the same molecules as Viton B except in slightly different amounts, therefore the Viton B reference is appropriate to use. The spectra collected from all over the Viton B600/SASN sample show that uniformity of dispersal was achieved in Fig. 54 and in the SEM analysis. The Raman bands from the Triton treated SASN and Viton B600 SASN are exactly the same showing the parent material, SASN, is consistent in molecular make-up.

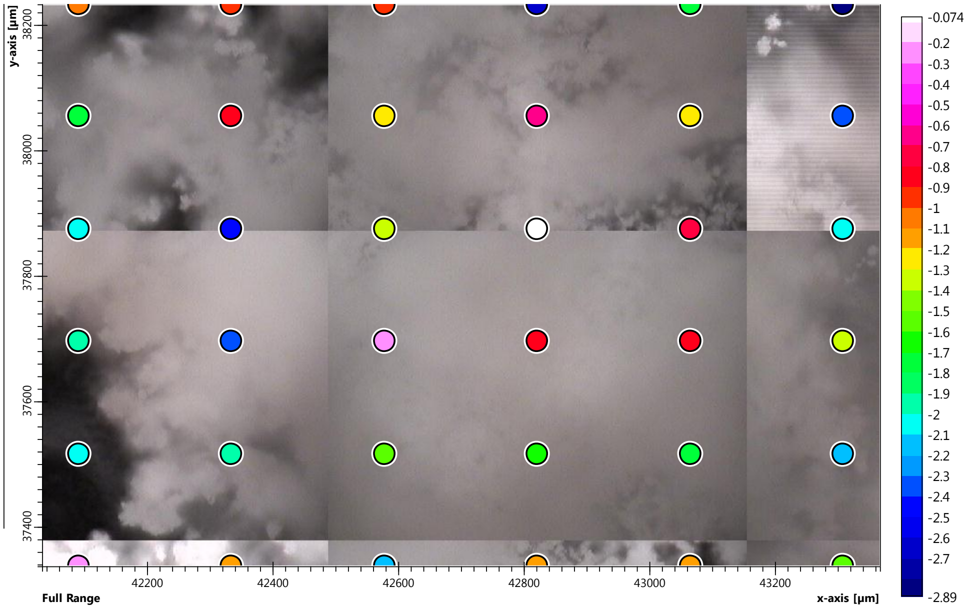

Figure 49, Actual map of probing areas for IR spectroscopy on the pure SASN sample. The out of focus areas show the relative surface topography [21].

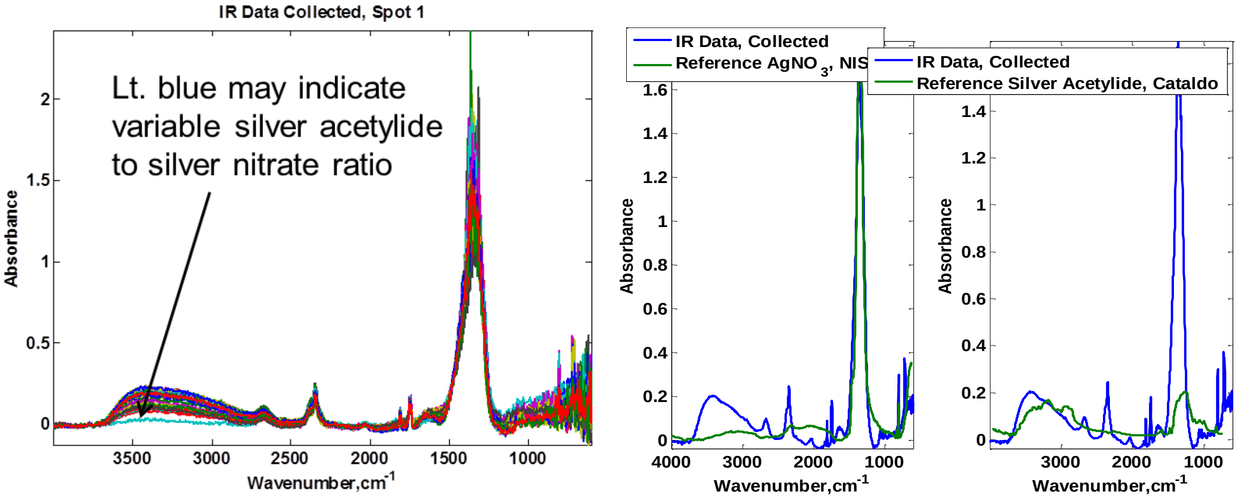

Figure 50, Infrared data of pure SASN from IR spectroscopy for test series TP49 on left [21] and TP48 on right. Notice the variation in absorbance intensity as pointed out in the left plot. The right plot is the averaged data (green traces) as compared to the NIST [28] and reference 29 from TP48, which was mapped out in Fig. 14 [22].

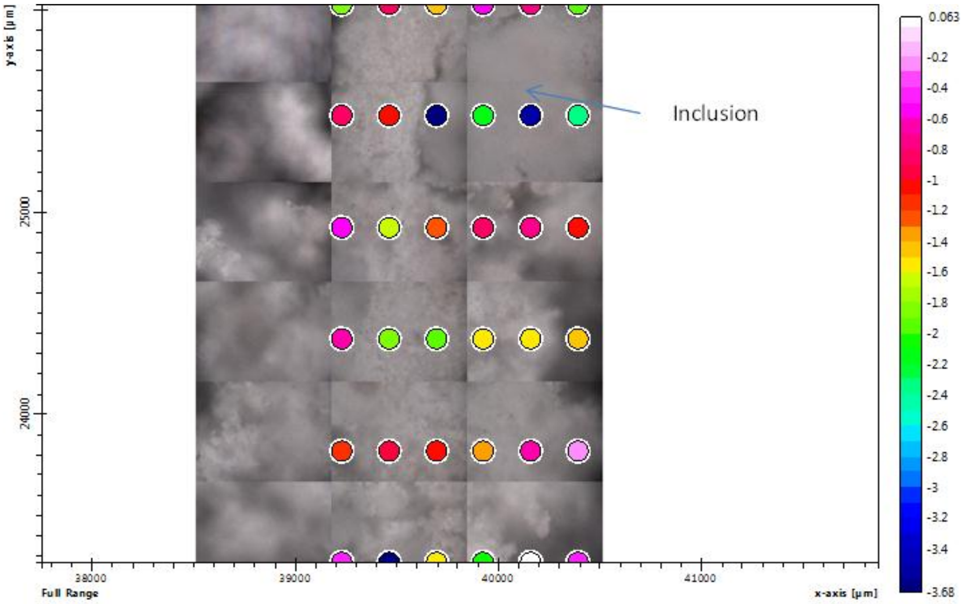

Figure 51, Triton X-100/SASN IR spectroscopy probing map. An inclusion is shown in the upper right hand corner and is thought to most likely be Viton B from the adherence layer [21].

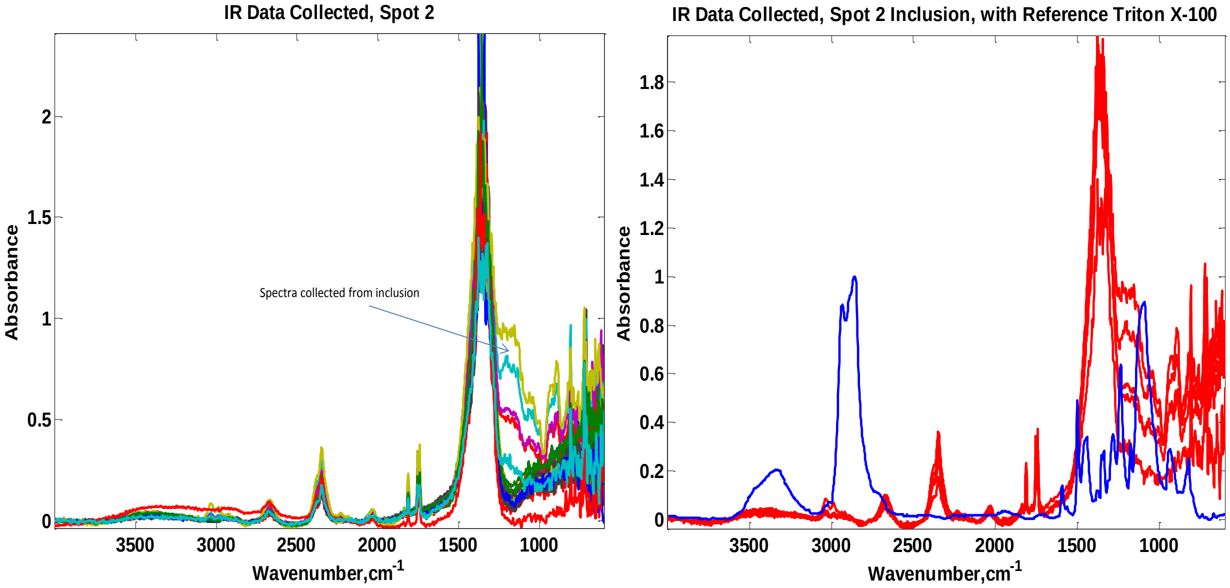

Figure 52, Collected IR data for the Triton treated SASN with a few of the spots showing the inclusion [21]. Right plot shows Triton X-100 reference [28] in blue against the averaged SASN data in a few red traces. This shows that the Triton X-100 was completely washed out of the SASN during the washing process.

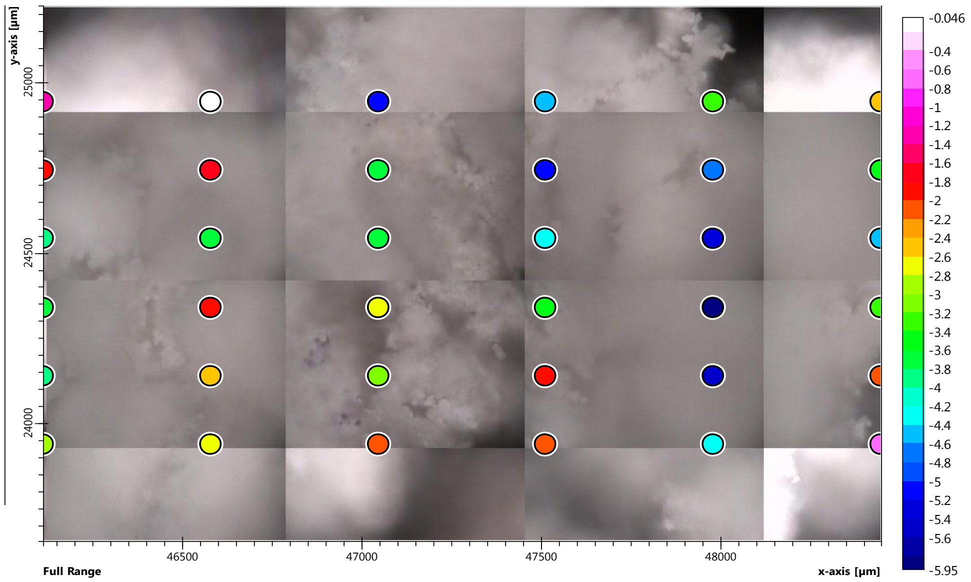

Figure 53, Actual map of probing areas for IR spectroscopy on the Viton B600 doped SASN sample. The out of focus areas show the relative surface topography [21].

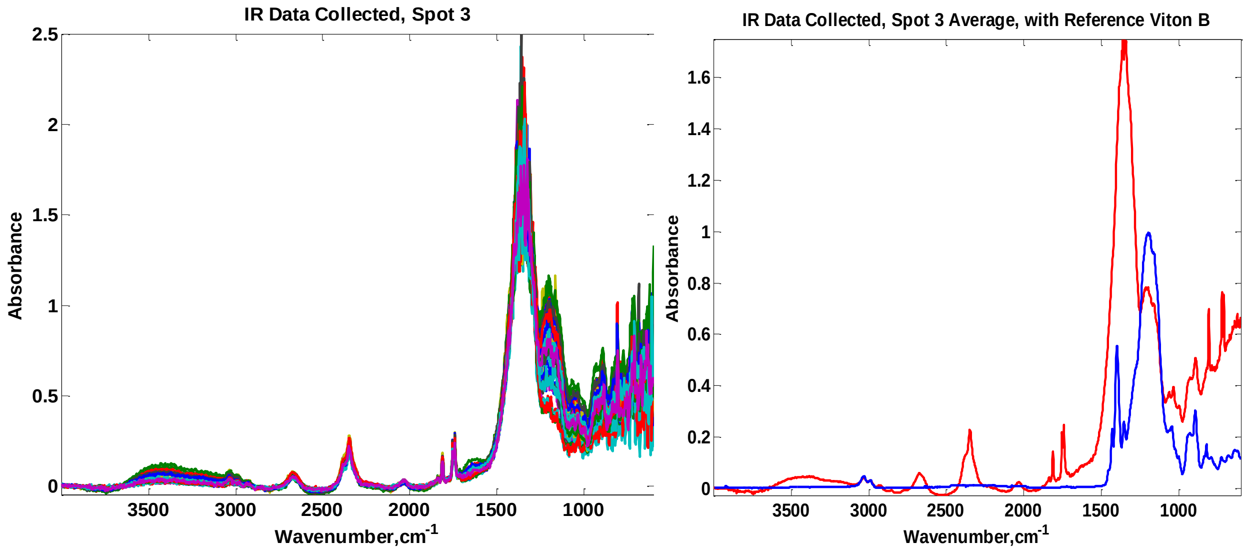

Figure 54, Left plot is all the collected IR data from the probing map of the Viton B600 doped SASN [21]. Right plot shows the great agreement in peaks between the Viton B reference [28] (blue trace) and the averaged Viton B600/SASN data (red trace). This data is a good indication of great dispersion of the Viton B600 dopant throughout the SASN matrix as also indicated in EDS data and SEM images.

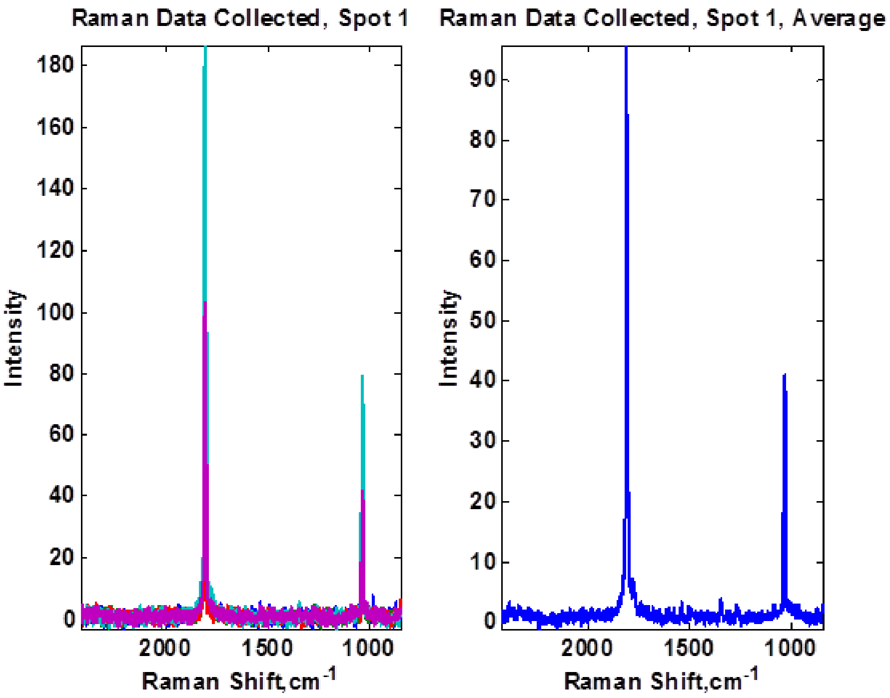

Figure 55, Left plot is all the collected Raman spectra from the five locations within the same pure SASN sample used in IR [21]. Right plot shows the average of the peaks. This data is a great because the Raman shifts are very distinct allowing unambiguous comparison with the reported SASN data.

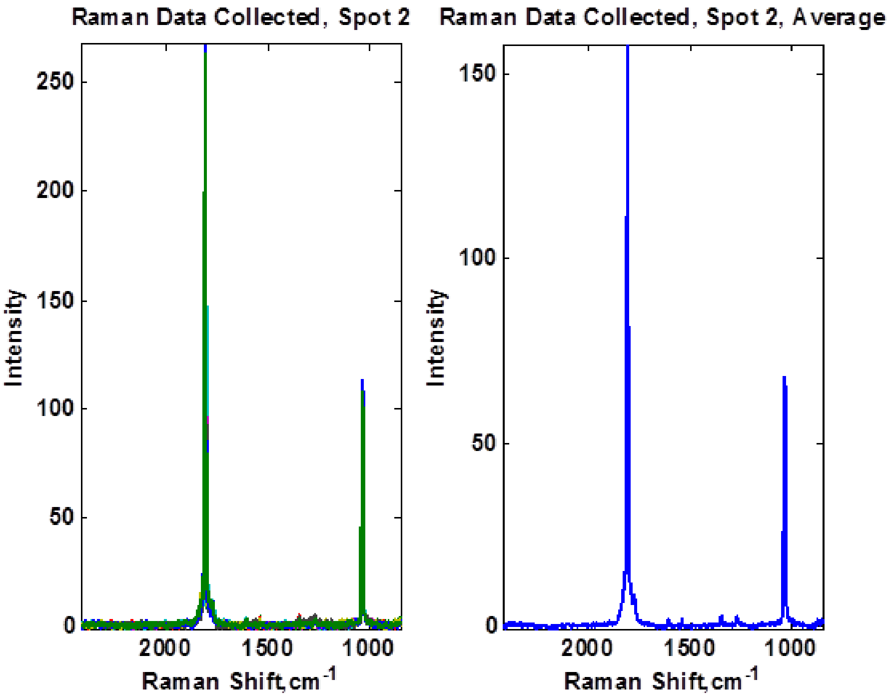

Figure 56, Left plot is all the collected Raman spectra from the five locations within the same Triton X-100/SASN sample used in IR [21]. Right plot shows the average of the peaks.

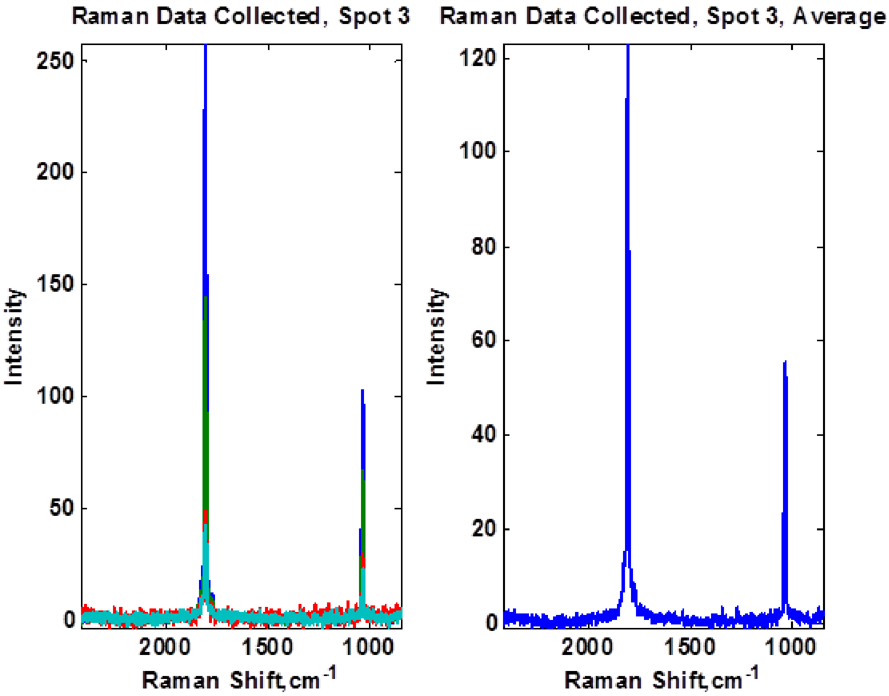

Figure 57, Left plot is all the collected Raman spectra from the five locations within the same Viton B600/SASN sample used in IR [21]. Right plot shows the average of the peaks.

CONCLUSIONS

Two new composite SASNs were formulated, sprayed, and tested with extensive characterization techniques. A standard control batch of pure SASN was used to compare the two composite explosives against and revealed that it was on the higher end of explosive output in terms of specific impulse and flyer plate velocity for an undetermined reason. Pressure spike measurements were made for the explosives tested, but the peak of the pure SASN and Triton treated SASN was missed and led to lower calculated pressure spikes inside the explosive as they detonated. However great data was collected for the pressure spike of the Viton B600 doped SASN giving an accurate measurement of the pressure spike of the explosive as it detonated.

Detonation/deflagration velocity was measured for the first time in the LIHE geometry, not the traditional sweeping wave down a track, and revealed the velocity of deflagration/detonation was a quarter the originally reported value. Also, the deflagration-to-detonation transition was measured for the first time for an LIHE and possibly for any primary explosive in this configuration. The DDT occurs roughly within 250-µm of the estimated ignition surface of the LIHEs tested in this study. Half of the explosive mass is deflagrating and supports claims made in another paper as to the effect to the explosive output in terms of maximum flyer plate velocity [1]. Also seen was either reflected shock waves propagating through the expanding combustion products or a retonation wave propagating through previously compacted and partially reacted explosive. Bulk density measurements indicated that the bulk densities of the composite explosives were indistinguishable from that of the normally produced SASN. The Viton doped SASN was from the same control batch, but the explosive output from it was significantly reduced. Thus, more explosive mass would be required to accelerate the flyer plate to higher velocities such as those for the pure SASN and Triton X-100/SASN.

Images of the explosives formulated showed that the microstructures were very similar, indistinguishable between pure SASN, Triton X-100/SASN, and Viton B600/SASN. Infrared and Raman spectroscopy indicated that the Triton X-100 doped SASN and control SASN are chemically the same, meaning the surfactant was washed out during the washing process. The addition of Triton X-100 during formulation did not seem to change the chemical make-up of the SASN. All three material characterization techniques agreed that the Viton B600 was contained in the SASN matrix and was well dispersed. Ion-beam nano-tomography was unachievable in the case of pure SASN and Triton doped SASN from TP49, but was achievable for pure SASN from TP48 and the Viton doped SASN in TP49. The pure SASN and Triton doped SASN both detonated during the cross-sectioning process and are thought to be much more sensitive than the pure SASN from TP48. Interestingly, pure SASN from TP49 was used to make the Viton B600/SASN and cross-sectioning was achievable. Viton B600 not only decreased the explosive output of pure SASN, but desensitized the explosive enough to allow ion-beam cutting.

ACKNOWLEDGMENTS

A special thanks to Kathy Alam and Laura Martin for IR and Raman analysis, Barry Ritchey for SEM, EDS, and ion-beam nano-tomography. Daniel Dow and Mike Willis are thanked for performing explosive operations as well as PDV and VISAR measurements. All the listed individuals input and help in determining the characteristics of SASN based explosives were greatly appreciated.

REFERENCES

1] Chavez, M.A., *Implications of Explosively Accelerating Thin Flyer Plates in the Transient Regimes of Explosive Systems: A Thesis, SAND2012-3438P, Unlimited Release.* Department of Mechanical Engineering. Socorro and Albuquerque, New Mexico: New Mexico Institute of Mining and Technology and Sandia National Laboratories, April 26, 2012.
2] Courtney-Pratt, J.S., Rogers, G.T., *Initiation of Explosion by Light and by Flying Fragments*. Nature 175, pgs 632-633, 1955.
3] Eggert, J., *The Initiation of Explosion by Light.* Proceedings of the Royal Society A246, pgs 240-247, 1958.
4] Eggert, J., *The Ignition of Explosives by Radiation.* Journal of Physical Chemistry 63, pgs 11-15, 1959.
5] Benham, R.A., *An Initiation and Gas Expansion Model for the Light-Initiated Explosive Silver Acetylide-Silver Nitrate.* Albuquerque, NM : Sandia National Laboratories, February 1980. SAND79-1829.
6] Wilden, M.W., *Investigations Pertinent to Ignition of Sprayed Layers of Silver Acetylide-Silver Nitrate.* Albuquerque, NM: Sandia National Laboratories, May 1986. SAND85-1859.
7] Baker, W.E., Hoese, F.O., Silverman, S., *Development of Capabilities of a Light-Initiated, Sprayed Explosive.* San Antonio, TX: Southwest Research Institute, September 1969. Technical Report IR Project No. 02-9008-08.
8] Johnson, R., *Final Report on SASN Investigation.* Phoenix, AZ: Unidynamics, February 26, 1987. Sandia Contract No. 04-1414, Document No. MCD-123.
9] Chung Wai Mak, T., Zhao, X., Wang, Q., Guo, G., *Structural Variation in Novel Double Salts of Silver Acetylide with Silver Nitrate: Fully Encapsulated Acetylide Dianion in Different Polyhedral Silver Cages,* Journal of American Chemical Society, Volume 121, pgs 3136-3141, 1999.
10] Covert, T.T., *Personal Communication.* Sandia National Laboratories, September 2010-March 2012.
11] Dolan, D.H., *Foundations of VISAR Analysis.* Albuquerque, NM : Sandia National Laboratories, April 2006. SAND2006-1950.
12] Jensen, B.J., Holtkamp, D.B., Rigg, P.A., Dolan, D.H., *Accuracy Limits and Window Corrections for Photon Doppler Velocimetry,* Journal of Applied Physics, Volume 101, 2007.
13] Strand, O.T., Goosman, D.R., Martinez, C., Whitworth, T.L., Kuhlow, W.W., *A Novel System for High-Speed Velocimetry Using Heterodyne Techniques.* Livermore, CA: Lawrence Livermore National Laboratories, November 2005. UCRL-JRNL-216919.
14] Willis, M.W., *Personal Communication.* Sandia National Laboratories, September 2010.
15] Souers, P.C. (technical editor), Owens, C. (production editor), *Lawrence Livermore National Laboratories Explosive Reference Handbook.* Livermore, CA: Lawrence Livermore National Laboratories, last updated April 2012. OUO.
16] Hargather, M.J., *Principles of Combustion Lecture Notes: Detonation Waves*. New Mexico Institute of Mining and Technology, December 2012.
17] Barker, L.M., Hollenbach, R.E., *Shock-Wave Studies of PMMA, Fused Silica, and Sapphire,* Journal of Applied Physics, Volume 41, Number 10, September 1970.
18] Ritchey, B., *Personal Communication.* Sandia National Laboratories, March-April 2012.
19] McDaniel, S., *Introduction to Energy Dispersive X-ray Spectrometry (EDS)*. University of California Riverside, Central Facility for Advanced Microscopy and Microanalysis, February 2, 2011, retrieved from: http://micron.ucr.edu/public/manuals/EDS-intro.pdf
20] Carter, E., *Vibrational Spectroscopy*. University of Sydney, Vibrational Spectroscopy Facility, April 21, 2010, retrieved from: http://sydney.edu.au/science/chemistry/spectroscopy/introduction/index.shtml
21] Alam, K. and Martin, L., *SASN Samples, Spot 1-3, Analysis Using Vibrational Spectroscopy*. Albuquerque, NM: Sandia National Laboratories, July 5, 2012. Memorandum.

22] Alam, K. and Martin, L., *SASN Analysis Using Vibrational Spectroscopy*. Albuquerque, NM: Sandia National Laboratories, May 7, 2012. Memorandum.
23] Ao, T. and Dolan, D. H., *SIRHEN:a Data Reduction Program for Photonic Doppler Velocimetry Measurements, SAND2010-3628*, Sandia National Laboratories, Albuquerque, NM, June 2010.
24] Benham, R.A., *Light Initiated Explosive Formulation and Impulse Calibration Procedures.* Albuquerque, NM: Sandia National Laboratories, April 7, 1977. Memorandum.
25] Richerson, D.W., *Modern Ceramic Engineering: Properties, Processing, and Use in Design.* Third Edition. Boca Raton, FL: CRC Press, 2006.
26] Guo, G.-C., G.-D. Zhou, and T.C.W. Mak, *Structural Variation in Novel Double Salts of Silver Acetylide with Silver Nitrate: Fully Encapusulated Acetylide Dianion in Differnt Polyhedral Silver Cages.* Journal of the American Chemical Society, 1998. 121: p. 3136-3141.
27] Alam, K., *Personal Communication.* Sandia National Laboratories, May 2012.
28] NIST. *Chemistry WebBook*. 2011, retrieved from: http://webbook.nist.gov/chemistry/
29] Cataldo, F. and Casari, C.S., *Synthesis, Structure and Thermal Properties of Copper and Silver Polyynides and Acetylides.* Journal of Inorganic and Organometallic Polymers, Volume 17: p. 641-651. 2007.